UNIVERSITY OF OKLAHOMA

GRADUATE COLLEGE

STATE-OF-THE-ART SCANNING ELECTRON MICROSCOPE FOR MULTIPLE APPLICATIONS: FROM SOLAR-CELLS TO MEGASPORES

A THESIS

SUBMITTED TO THE GRADUATE FACULTY

in partial fulfillment of the requirements for the

Degree of

MASTER OF SCIENCE

By

CÉDRIC CORRÈGE
Norman, Oklahoma
2016

STATE-OF-THE-ART SCANNING ELECTRON MICROSCOPE FOR MULTIPLE APPLICATIONS:
FROM SOLAR-CELLS TO MEGASPORES

A THESIS APPROVED FOR THE

DEPARTMENT OF ENGINEERING PHYSICS

BY

Dr. Matthew B. Johnson, Chair

Dr. Michael B. Santos

Dr. Sheena Murphy

Acknowledgements

It is customary to acknowledge people who supported you during your work. My thesis is not an exception and I would like to express my gratitude to the people bellow, but also to everybody I might have forgotten; this is not only my accomplishment, but also the one of all the people supporting me. I would not have achieved this much without you all!

People from the United-States:

My first acknowledgement goes to Prof. Michael B. Santos for accepting me in the engineering physics double degree program.

I want to express my deepest gratitude to Prof. Matthew Johnson for his great advising and support, without whom finishing this degree would have been difficult.

My kind regards to Prof. Sheena Murphy for being part of my committee and supporting me as a T.A.

A special thank you to Dr. Preston Larson for teaching me electron microscopy and his continuous advises.

I am also grateful to Joseph Tessmer, for helping me using the AFM.

I would like to thank Amy Shaw, for helping me with the administration.

Thank you to all the friends I met in Oklahoma; this part of my life would have not been the same without you.

Finally, thank you Esther Williams, my lovely Tex-Mex. The U-S is not the same since I met you.

People from France:

I would like to say "merci" to Prof. Jean-Pierre Fontaine from Polytech Clermont-Ferrand for helping me from France during my stay at OU.

Thank you Prof. Bernard Gruzza and Joël Leymarie for being part of the French committee.

A thank you to my friends from France, I am lucky to have all of you in my life and cannot wait to see you.

Miss. Figeac, you will likely never see these words, and I probably should not write them, but this list would have been greatly incomplete without you; thank you for everything.

Finally, I would like to thank my parents, my sister and grandparents for their unconditional love, financial and moral support and the life I had. I owe you everything.

Contents

List of Tables

List of Figures

Acronyms

O_2 dioxygen. xi, 37, 39

μm micrometre. 67, 75

nm nanometre. xiii, 46, 55, 73, 75, 79, 81

pA picoampere. 75

1D one dimensional. 28

2D two dimensional. 33

3D three dimensional. xiii, 17, 33, 75, 76, 79, 81, 82, 84

AFM atomic force microscopy. x, xii, 15–20, 22, 28, 30, 33, 40, 41, 46, 50, 57–63

Al aluminium. 8

Ar argon. xi, 39, 63

As arsenic. 6, 8, 10, 14, 15, 30, 63

ECCI electron channelling contrast imaging. 48, 49

EDS energy-dispersive X-ray spectroscopy. xi, xiii, 38, 82, 83

FIB focused ion beam. xiii, xix, 48, 53–55, 67, 70, 72–77, 79, 84

Ga gallium. 6, 8, 10, 14, 15

IB intermediate band. x, 6, 14, 63

In indium. 6, 8, 10, 15, 30, 63

MBE Molecular Beam Epitaxy. 10

N nitrogen. 8

NIST National Institute of Standards and Technology. 37, 39

OU the University of Oklahoma. xix, 15, 17, 33, 43, 48, 50, 70

P phosphor. 8

PL Photoluminescence. 15

PV photovoltaic. 2–7, 11, 13

QD quantum dot. x–xii, xix, 6, 7, 9–11, 14, 15, 17, 19–22, 24–28, 30–32, 35, 36, 40–44, 46–50, 57–60, 62–64

RHEED reflection high-energy electron diffraction. 31, 61

Sb antimony. xi, 6, 8, 15, 27, 41, 63

SE secondary electrons. xiii, 34, 49, 60, 75, 82

SEM scanning electron microscopy. xii, xiii, xix, 16, 19, 33, 34, 38, 40, 41, 43, 46–48, 50, 57–63, 69, 70, 72, 74, 76, 84

Si silicon. 4–6

STM scanning tunnelling microscopy. 46

TEM transmission electron microscopy. xii, xix, 15, 46, 50–55, 57, 62–64, 70, 84

W tungsten. 53

WD working distance. 34, 36

Abstract

The University of Oklahoma (OU) recently acquired a Zeiss Neon, a dual beam SEM/FIB Cross beam machine. This thesis focuses on its utilization via two independent projects, one involving the characterization of solar-cells semiconductor materials while the other focuses on the FIB to provide information about a preserved megaspore.

Part I: Solar-Cells

Third generation photovoltaics (PVs) seek to increase the efficiency of PVs and reduce their cost. One candidate to this third generation involves the use of quantum dot (QD) structures to create an intermediate band-gap. This device can overcome the Shockley-Queisser efficiency limit (about 30%) by better utilizing the solar spectrum. However, the current results are far from the theoretical limit, partly because of the material quality of the QDs structure. This project involves high-density self-assembled $InAs/GaAs_{1-x}Sb_x$ QDs grown by molecular beam epitaxy at the University of Oklahoma (OU). Ultimately, size, shape, density, composition, and crystalline quality of the QDs as well as similar details for the matrix layers play an important role in the PV efficiency. Hence, the characterization of these properties is important. Characterizing multiple layers of QDs will ultimately require cross-sectional transmission mi-

croscopy; however, along the way, atomic force microscopy (AFM) and field-emission scanning electron microscopy (FE-SEM) will more easily yield details about the uncapped top QD layer. For example AFM accurately determines QD density, and quantitatively describes QD shape. On the other hand, AFM is sensitive to tip/probe-shape artifacts. Cross-sectional FE-SEM can clear up some of these artifacts and indicate crystalline quality; cross-sectional FE-SEM was found as a means of giving better lateral resolution than our typical AFM results. Ultimately, cross-sectional images from a transmission electron microscope (TEM), would provide the best information, however pitfalls and machine breakage delayed us in our work; while SEM/FIB in situ TEM preparation is now possible, it could not be operated

Part II: Megaspores

Optical and electron microscopy are critical tools for studying preserved and fossilized organisms. Due to its early development and refinement, light microscopy has dominated the study of organic-walled fossils. Taxonomic identification and discrimination is almost exclusively based on features visible under transmitted light. However electron microscopy, and in particular TEM, has been applied to investigations of the ultrastructure of the walls and ornament that are beyond the resolution of light microscopy. Hypotheses for the assembly of the walls have been formulated based on these data. Recently new techniques, such as FIB, SEM, and synchrotron radiation tomography, have expanded the boundaries of imaging fossils. This thesis part focuses on investigating Arcelites Hexapartitus species megaspore, using an SEM with FIB to obtain three dimensional information about their inner exine channels. Channels were readily imaged through the inner exine using a number of cross-beam geometries. The channels seem to be simply connected running through the inner part of the exine layers, how-

ever, the channels/pores are found to stop before exiting this inner exine layer at both its inner and outer surfaces. Additionally, it was found that they are not continuous this inner exine layer. Investigations concerning the material obstructing the channels have begun. So far, there is no evidence of a foreign material present. It appears that the pores simply end before exiting the layers and have occasional nano sized regions of sporopollenin, the megaspore wall material, blocking the channels.

Preface

The University of Oklahoma (OU) recently acquired a Zeiss Neon EsB dual beam SEM/FIB Cross beam machine. In addition to providing excellent resolution, other accessories can be added to broaden the microscope's functionality. However, very few of these functions are ever used. This is partly due to a lack of communication regarding the functions and a lack of experience on how to operate them. During this thesis, two of these functions were studied independently during two different projects.

The first project involves the use of a micromanipulator in order to operate in situ TEM sample preparation. This was done through the characterisation of QD material for solar cell application. This section was very interesting and pleasant and is referred as part I : SEMper TEMpus fugit.

The second function that was studied is the three dimensional reconstruction of the entine of a "fossil" megaspore. This was done by slicing the spore with the FIB while taking images with the electron inlen detector. This is referred as part II : Another FIB Usage: 3D Reconstruction.

Part I

SEMper TEMpus fugit

Chapter 1

Introduction

The last century considerably transformed our way of living with the democratisation of electricity. Now, other continents, and especially Africa, are facing substantial economic and demographic growth which can only be sustained by making major investments in the energy sector. [10] The petroleum crisis that began in 1973, was the first sign indicating that the world could not rely solely on fossil fuel energy. Since then, many geopolitical events, including the recent crisis in the middle east, confirm the need of active development of alternative renewable energy. Furthermore, the effects of the now-acknowledged global warming crisis, partially due to carbon emissions, are important to the international community. Theis concerns were publicly expressed during the 21^{st} United Nations Climate Change Conference held in Paris in November, 2015 ([11]). There, they agreed that there is a growing need for the development of renewable resources. This is why much current research is focused on renewable energy including wind energy, biomass energy, hydroelectric energy, and others. This thesis focuses on new materials for photovoltaic (PV) devices that harness solar energy.

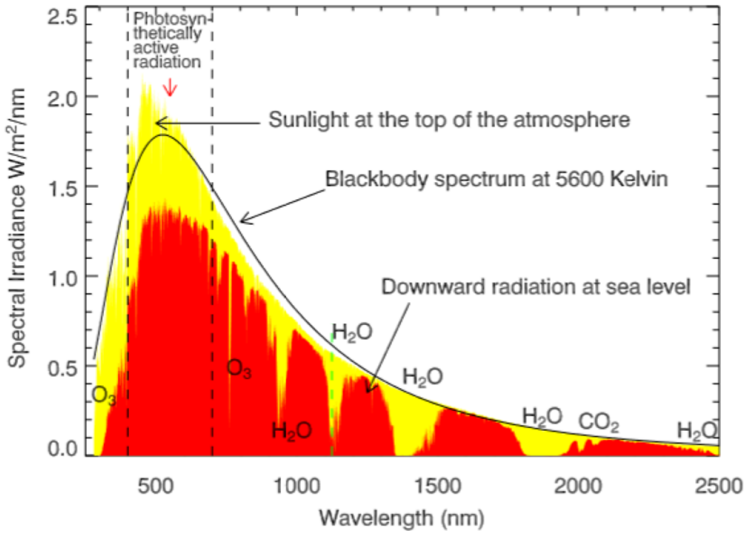

Figure 1.1: The solar radiation spectrum at the top of the atmosphere, Earth surface and the black body approximation. [1]

The Solar Resource

The Sun is a huge ball of plasma that has been providing most of Earth's energy for billions of years. The surface of the sun, called the photosphere, can be well approximated as a black body with a temperature of around 6000 K that radiates into space (c.f. Figure 1.1). Using the inverse-squared rule, Earth receives about 1.7×10^{17} Watts from the Sun's radiation. Only about 36% of this power reaches the surface of the Earth, providing us with a power density of about 1367 $\mathrm{W} \cdot m^{-2}$. This is called the "solar constant" [1]. Thus, the energy provided by the sun is about $3.3 \times 10^{24} J/year$. This currently represents about 6800 times our yearly energy consumption. This energy can be converted into different forms of energy —mainly electricity and heat. However, even if the energy provided by the the sun is gargantuan, it is useless if we do not have efficient ways to convert it into usable forms. This is where the different generations of photovoltaic (PV) cells become necessary. The next section will

describe the changes that occurred within each generation of PV devices.

Photovoltaic Devices

PV is a method that transforms electromagnetic radiation into electricity. PV is a convenient technique since it does not make any noise, lasts for years, and thus can be integrated into our architecture without major issues.

Brief History

The PV effect was discovered by the French physicist Alexandre Edmond Becquerel in 1839. However, the first PV device is attributed to Charles Fritts in the early 1880s. He created his PV device by melting a selenium film onto a thin gold layer. Unfortunately, the low efficiency and high cost of the cell prevented it from use in any application[12]. The first major breakthrough in solar cell fabrication was achieved in the 1950s with the use of silicon (Si). Si drastically increased the efficiency of solar cells up to 6% [13]. At the time, solar cell applications were not obvious. Solar cells were primarily used as a power supply for satellites. Humanity waited until the oil shortage during the petroleum crisis of the 1970s to recognise the growing need of alternate energy sources. This prompted the investigation of PV devices. In 1985, research on Si solar cells began to rapidly pay of when an efficiency of 20% was achieved for the first time[14].

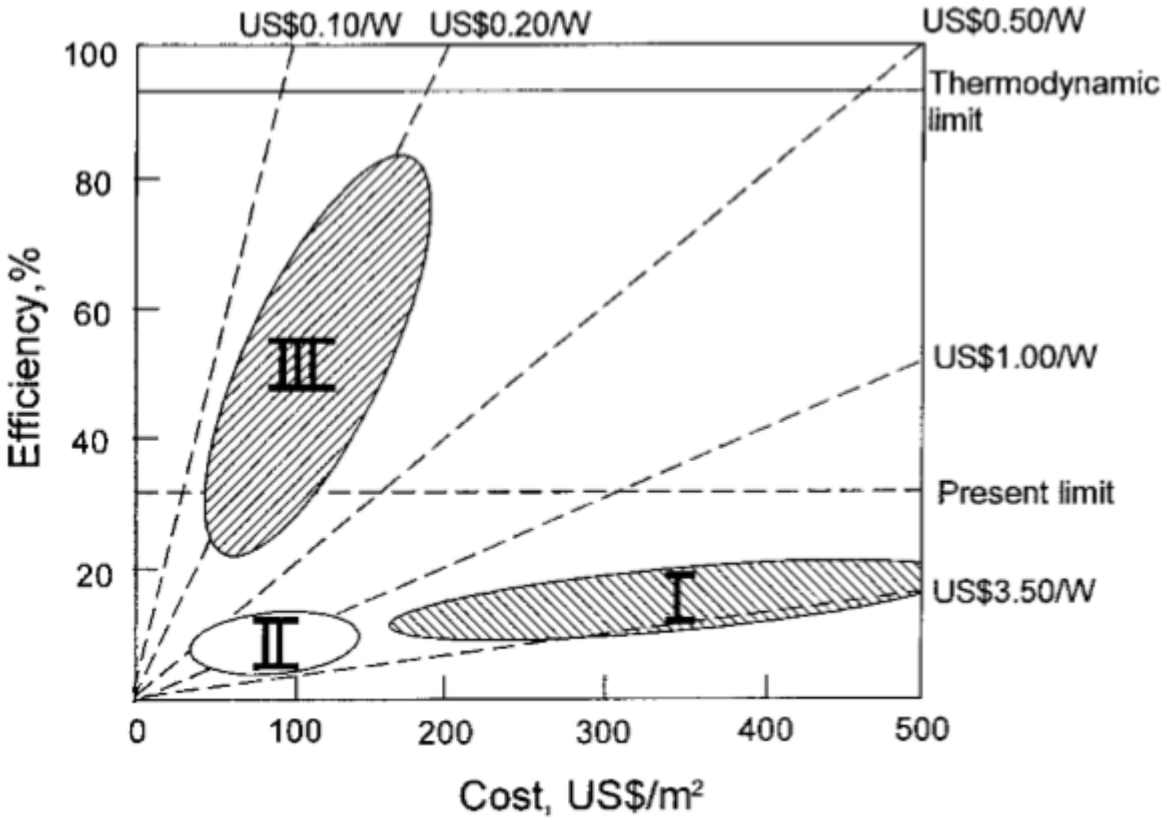

Figure 1.2: Efficiency and cost projections for the first, second and third generation of photovoltaic technology [2].

Photovoltaic Generations

Different technologies, including bulk Si, III-V materials, and even organic material, have been used to build PV devices. Experts divided solar cell technology into three generations which are summarised in Figure 1.2. The first generation, which still represents most of the market, is characterised by its high manufacturing cost for middle efficiency bounded by the Shockley-Queisser limit (30%) [15]. Second generation solar cells are often referred as thin films due to their small thickness which varies from a few nanometres to tens of micrometres. Therefore, they are lighter, flexible, semi-transparent and thus can easily be

integrated in human buildings. Additionally, thin films are cheaper to produce, with the cost per watt continually decreasing with the increase of efficiency. However, they are less efficient and can contain toxic materials, like cadmium unlike traditional PV devices.

Historically, Si was used to make PV devices. Studies have shown that Si has a bandgap close to the optimal one needed for homojunction solar cells. If Gallium Arsenide (GaAs) is a more efficient material for homojunction cells [16]. But its costs are still too high to be competitive, needing one to rethink PV design. The third generation aims to drastically cut the cost per watt and improve the efficiency. This generation is still under active development. Many designs, such as organic solar cells, tandem cells and IB cells are being proposed[2, 15]. Figure 1.2 summarises the differences between the three generations of solar cells.
This thesis focuses on material for the third generation of solar cells, and more specifically, IB PV cells where the IB is achieved by using an array of quantum dot. The materials involved are indium (In) arsenide QDs within a gallium (Ga) Arsenide Sb matrix, which will be described in detail further on in this thesis.

Chapter 2

Technical background

Now that we know more about the history of solar cells, we will focus on the physics of QDs. In this section, we will describe the theoretical concepts involved in PV that one needs to know in order to understand the work presented later.

Semiconductors in solar devices

Semiconductors are the basis of solar cells. Let's work through its definition and general consideration explaining the physics behind them. Figure 2.1 can be used to briefly describe the differences between conductors, semiconductors and insulators. In conductors (e.g. metals), the conduction and valence bands overlap, making it unnecessary for electrons to transit from one band to the other. In insulator, the bandgap is large enough to prevent visible light from energy transitions across the bandgap. In semiconductors however, the bandgap is narrow ($\sim$1eV) making it possible, to excite an electron from the valence band to the conduction band by absorbing a photon of visible light. When the electron

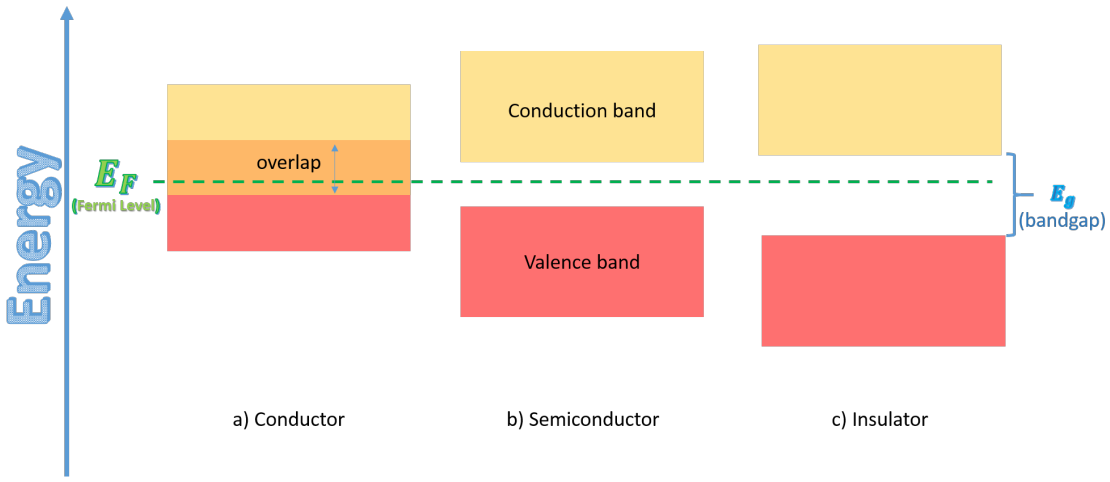

Figure 2.1: Conductivity of solids, categorised in terms of their energy bandgap

leaves the valence band, an empty state (or "hole") is left behind. The creation of an electron-hole pair is called an exciton.

III-V materials are crystalline semiconductors made of atoms from the group III (mainly Aluminium (Al), Ga and In) and group V (mostly Nitrogen (N), Phosphor (P), Arsenic (As) and Sb) element from Mendeleev's periodic table. They usually form a zinc blende crystal structure.

III-V materials receive plenty of attention because of their unusual properties. First of all, some components, including GaAs, InAs and InSb, have a high electron mobility, essential in high speed operations. Furthermore, most III-V materials have a direct bandgap that makes them efficient absorbers and emitters of light. This is an important property that broadens the path towards to optoelectronic applications. The different possible alloy combinations allow one to perform "bandgap engineering" (for instance in tandem cells) which provides a fairly broad range of accessible light wavelength. One can get an idea of the accessible bandgaps from Figure 2.2.

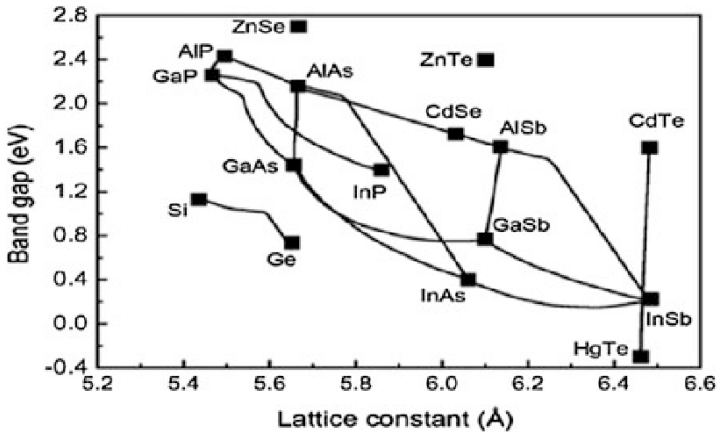

Figure 2.2: Energy bandgap as a function of the lattice constant for some III–V and II–VI semiconductors [3]

Quantum Dots as Semiconductors

QDs are nano-mono-crystals. Due to their small size, smaller to the exciton Bohr radius, they acquire confinement properties. Indeed, QDs can be understood using the textbook case "particle in a box" which explains its alternative name : artificial atom.

Because the exciton is confined in a space smaller than the Bohr radius, the QDs act like macromolecules. Any change in the number of atoms (i.e. size) results in a change in the bandgap energy. Studies have shown that an increase in size leads to a redshift of the wavelengths associated with the QD [17]. Bruce introduced an equation (Equation 2.1 [18]) that predicts this behaviour and links bandgap to radius of curvature in QDs.

$$\Delta E_{QD}(R) = E_{bulk} + \frac{h^2}{8R^2}(\frac{1}{m_e^*} + \frac{1}{m_h^*}) - \frac{1.786e^2}{4\pi\epsilon_0\epsilon_r R^2} \tag{2.1}$$

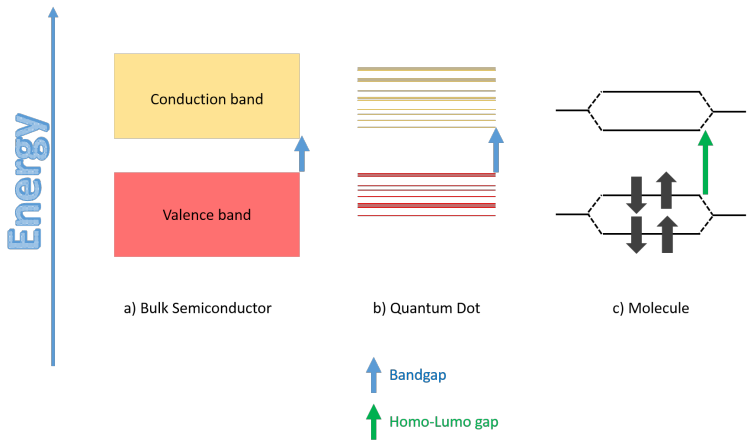

Figure 2.3: Comparison of bulk semiconductor, quantum dots and molecule band structure

This particularity is quite handy in bandgap engineering and has lead to different methods for creating QDs. Two general strategies have been used to manufacture QDs —the top-down and the bottom-up approaches[19]. The top-down approach consists of nano-scale patterning. Nano-scale patterning involves starting from crystals and molding them to desired shapes. Electron beam lithography and photo-lithography are generally the techniques used for patterning. The bottom-up approach is more common and generally provides a higher density of QDs. It consist in agglomerating atoms to form the desired structure, often through the use of Molecular Beam Epitaxy (MBE). The MBE process builds a crystal by adding atoms layer-by-layer. To obtain QDs, the Stranski-Krastanov method is used. It consist in depositing one material (for instance, InAs) on top of another material (e.g. GaAs) with a slightly different lattice constant. The strain created by the lattice-mismatch drives the creation of small islands —these are QDs. Figure 2.4 a) schematically shows the Stranski-Krastanov method. Figure 2.4 b) qualitatively illustrates the stress building up, creating the QDs. The growth conditions are very important and

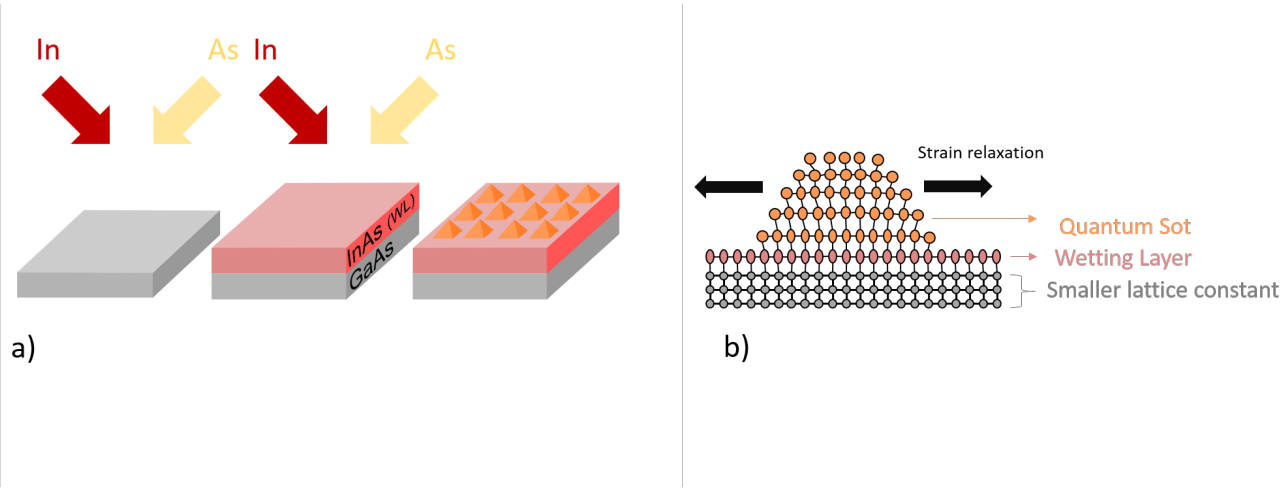

Figure 2.4: a) Stranski-Krastanov growth scheme b) Qualitative view of a QD with internal strain

small changes to any of the parameters (temperature, waiting time, flux, lattice mismatch, etc.) can drastically change the QD size, shape and density; these parameters will be crucial to the final efficiency which affects the cost per Watt of the cells.

Solar cell physics

PV devices are made of semiconductors and use light as the the energy source to create excitons, which quickly dissociate into a free electron and free hole. This section focuses on the physics of PV devices.

Propagation of light

Maxwell's equations describe the behaviour of electromagnetic waves. While the solution to these equations is easy to obtain in free space, where one obtains planar waves (perpendicular oscillating fields moving in one direction at

speed of light), it is more complicated to find the solution in solids. The interaction with conducting matter leads to a damping therm. A damping term is a modification of the speed based on the wave frequency and the solid refractive index. Sometimes, the interaction with non-dielectric matter can also lead to a break in the perpendicularity of the fields.

When an electromagnetic wave goes from one medium to another, a fraction of the wave is transmitted and the other fraction is reflected. This behaviour is described by Fresnel's equation (Equation 2.2)

$$\begin{cases} r = \frac{E_r}{E_i} = \frac{n_1 - n_2}{n_1 + n_2} \\ t = \frac{E_t}{E_i} = \frac{2n_1}{n_1 + n_2} \end{cases} \tag{2.2}$$

Respectively, E_i, E_r and E_t are the electric field amplitude of the incident, the reflected wave and the transmitted wave. $\widetilde{n_1}$ and $\widetilde{n_2}$ are the complex refractive index of the first and second media. The intensity of the waves are given by the reflectance $R = |r|^2$. If the first medium is a vacuum (or air), $\widetilde{n_1} \approx 1$ and $\widetilde{n_2} = n_r + in_i$ then, equation 2.2 can be written as:

$$R = \frac{(n_r - 1)^2 + n_i^2}{(n_r + 1)^2 + n_i^2} \tag{2.3}$$

Unfortunately, The reflection coefficient is typically important in semiconductors ($\sim 40\%$) since they often have a high refractive index (~ 3). One must then find other ways to increase this coefficient and obtain efficient light absorbers. The transmitted part is more complex; in semiconductors, as in conductors, the intensity is damped because energy is transferred to the crystal. One can write :

$$I_t = I_i e^{-2\kappa z} = I_i e^{-\frac{z}{\delta}} \tag{2.4}$$

Where κ, the so called extinction coefficient, is the complex part of the wave vector, $\widetilde{k} = k + i\kappa$ and δ the skin depth or penetration depth. δ represents the distance it takes to reduce the intensity by a factor of $1/e \approx 1/3$. If the transmitted wave energy is higher than the semiconductor bandgap, an exciton can be created and the surplus of energy is converted into heat.

The homojuction cell

Once the light penetrates our sample, it interacts with it. This section presents the homojucntion solar cell's physics —the most basic PV device.

The single junction solar cell is a simple p-n junction. The n and p doping creates a depletion zone where carriers are removed and the remaining ions create an electric field. When light strikes the crystal in the depletion zone with sufficient energy, it creates an exciton. The electric field separates the electron from the hole. The electrons in the so called conduction band move in one direction while the holes in the valence band, move in the opposit direction. This can be schematised as a two band diagram.

With a continuous amount of light striking the crystal, a difference of potential is created allowing electric work to be provided if any device is connected to the cell.

Quantum Dots Solar Cells and Project Advancement

Showing promising results, the homojunction solar cell was used in the first generation of PV devices. A lot of studies were done on homojunction cells and it was found that the maximum efficiency, called the Shockley limit, was

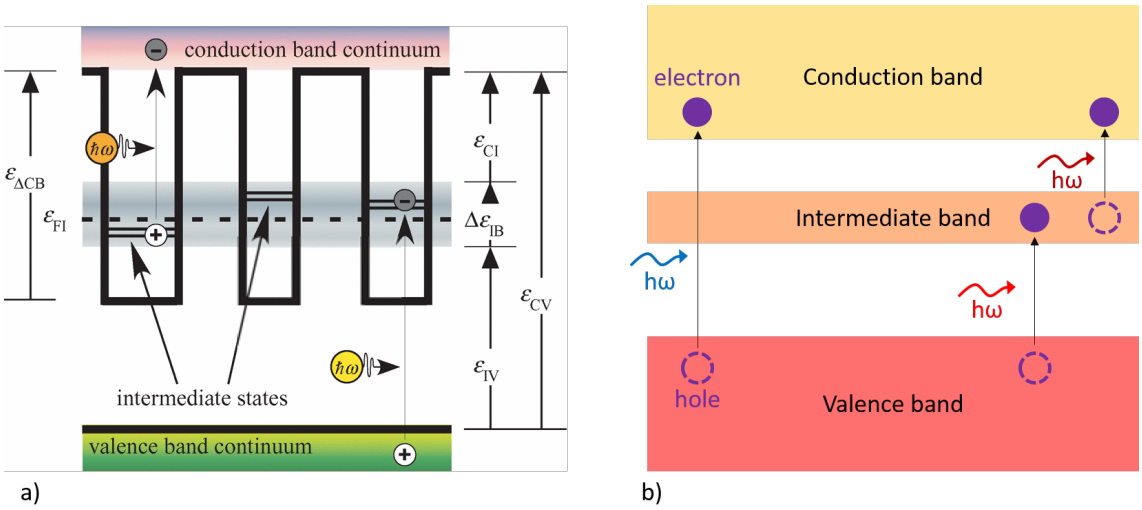

Figure 2.5: Intermediate Band Solar Cell Energetic structure of an IB solar cell of non-uniform QD heterojunctions. The minimum energy needed to excite an electron from the intermediate states to the conduction band and from the valence band to the intermediate states are ϵ_{CI} and ϵ_{IV}, respectively. This intermediate states can be describe by a quasi-Fermi level : $\epsilon_F I$ [4].

around 30% [15]. To overcome this limit, new designs needed to be proposed. One design that is currently being proposed is the IBQD. The idea in IBQD is to increase the cell efficiency by adding another band. This would allow photons with three different wavelengths to be absorbed (c.f. Figure 2.5). In most approaches, including the one outlined here, stacked arrays of QD are used to create this IB. Those QDs are addend in the depletion zone, and their quantum confinments effect allows additional available states to be ocupied by carriers. These states width is define by the uniformity of the QD layer and —assuming all the carriers in the intermediate states are in electrochemical equilibrium— their occupancy statistics may be described by a single quasi-Fermi level ϵ_{FI} [4].

To increase the absorption, several layers within the penetration depth of light must be built.[1] However, increasing the number of layers increases the strain

[1]The penetration depth can be quite short. In this study, for instance, GaAs's penetration depth for the incident light, having a wavelength of 540 nanometres, is 93 nanometres. [20]

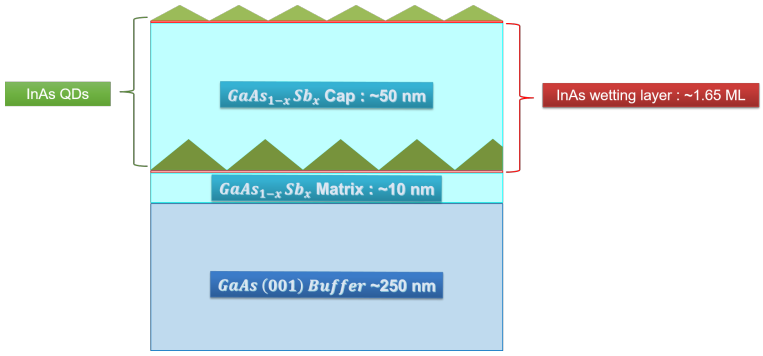

Figure 2.6: Layer structure for QD samples, from [5]

within the material. This affects the material's absorption and conduction [21]. Therefore, increasing the number of QD layers is not always beneficial. Indeed, an experimental study has shown that —for InAs QDs on a GaAs matrix— increasing the number of layers from 10 to 20 to 50 decreases the cell performance [22]. This is why Levy and Honsberg proposed some stress compensation material [4]. However, introducing Sb changes the confinement potential and can lead to a type II band alignment [23]. OU is currently studying such materials and has grown several sets of InAs on a $GaAs_{1-x}Sb_x$ matrix. The composition of the sample is described in figure 2.6. The shape and density of the QDs was significantly influenced by the concentration of Sb, needing one to characterise those materials. Photoluminescence (PL) measurements and AFM were used on these samples to compare them [24]. The T657 sample featuring 13% of Sb, seemed to possess the best properties. PL provides different types of information. The height of the PL peak gives us an idea of the density of the QDs, the position of the peak gives us an idea of the size of the QDs, and the width of the peak gives us an idea of the distribution of the size of the QDs. However, more quantitative information is needed regarding the shape of such materials in order to enhance the growth method. Ultimately, TEM would provide the best information; however, it is a very time consuming process. This is why

obtaining similar information with AFM and SEM was investigated.

Chapter 3

Atomic Force Microscopy

In order to obtain information such as the density, the shape and the volume of the QDs, AFM was firstly used. AFM is a fast and convenient (vacuum-free) technique that allows one to obtain 3D pictures of a surface morphology. Globally speaking, it consists of scanning the sample with a sharp tip on the end of a flexible cantilever. The tip-sample interaction is monitored by a laser and provides topological information. There are three ways of operating the machine; the contact, tapping and non-contact modes. The contact and tapping modes are more precise and generally used more often than the non-contact mode, however, the sample and the tip can be damage during the operation. This is why we choose to work with the non-contact mode.

In this section we will describe the work done with the OU AFM; an Asylum Research MFP-3D-Bio using a Asylum AC160TS-R3 (9 ± 2 nm radius) tip. The three samples of interest were imaged, however, sample T788C1 did not look as expected and could not be used in this study.

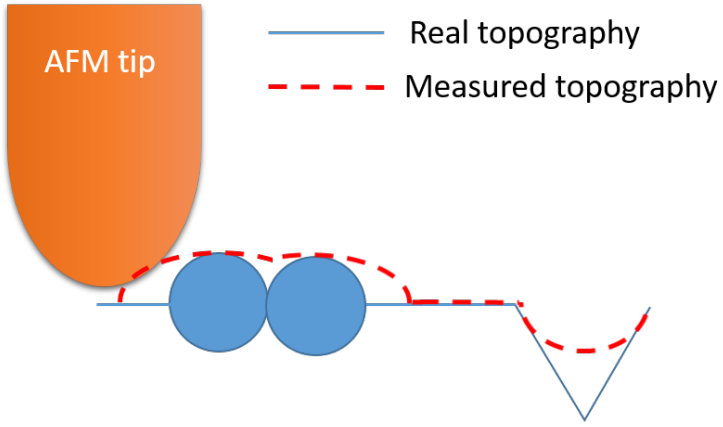

Figure 3.1: Schematic illustrating AFM tip artifact

Data extraction

Since AFM pictures are a measure of the tip-sample interaction, the raw pictures do not represent the sample but rather a convolution of the tip and the topographic information. Figure 3.1 present three consequences of this artifact with a relatively "dull" tip. Trying to characterise raw data would result in an underestimation of the height and depth. On figure 3.1, it can be see that the feature size are not correctly recorded. Indeed, the feature's diameter is overestimate and an inattentive eye might count one sphere instead of two. This is why one must be careful regarding the raw data and apply several corrections.

Extraction Protocol

Gwyddion [25] —probably the best AFM free software available— was used to extract and filter the data. The following protocol was used :

1. Align rows using matching
2. Correct horizontal scars (stocks)

3. Level data to make facets point upward

4. Level data by mean plan subtraction

5. Remove polynomial background (3^{rd} degree)

6. Shift minimum data value to zero

7. Blind tip estimation

8. Surface reconstruction

The blind tip estimation was used which might be a problem. Figure 3.2 presents images of T657 with (a) a simple shift, (b) before convolution and (d) after surface reconstruction. In this picture, one can observe that the maximum height of the sample is decreased during the data processing. To further analyse this behaviour, Figure 3.4 showing the maximum height, average height and average QD height in several samples can be used. Surprisingly, the maximum and average quantum QD height is decreased by the deconvolution; however, the surface reconstruction does not seem to have an important impact. Most of the changes are due to the filters applied to the sample. The shape of the AFM probe was verified using SEM; Figure 3.3 shows a new tip and one after being used on a sample. The radius seems to be within the lower end limit of the

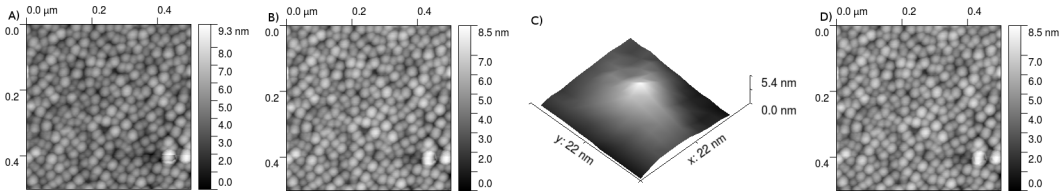

Figure 3.2: AFM picture of T657 sample extracted differently. A) the data presented with just a shift so that the minimum value is zero, B) the data after going through step 1 to 6, C) the blind estimation of the tip and finally, D) the data after the surface reconstruction.

specifications, but the used tip shows some severe damages. Because of those damages, the blind tip approximation was preferred to using the original shape; Those damages might also explain the unexpectedly dull shape of the tip in the blind tip approximation.

Data processing

Once the data are properly extracted, information can be retrieved. However to do so, one must have the right tool. In this sample we are particularly interested in the QD size (i.e. height and diameter), shape (i.e. radius of curvature) distribution as much as the density. Different attempts were made using Gwiddion or imageJ but none seems to be quite automatic, reliable and easy to use. Different parameters have to be tweaked needing one to constantly check if the output is correct. For instance with Gwyddion the best algorithm appears to be the watershed, but it is really inconsistent providing sometime a 30% error and sometimes being an order of magnitude out (detecting multiple QDs in one). ImageJ was not studied thoroughly; the approach was to threshold

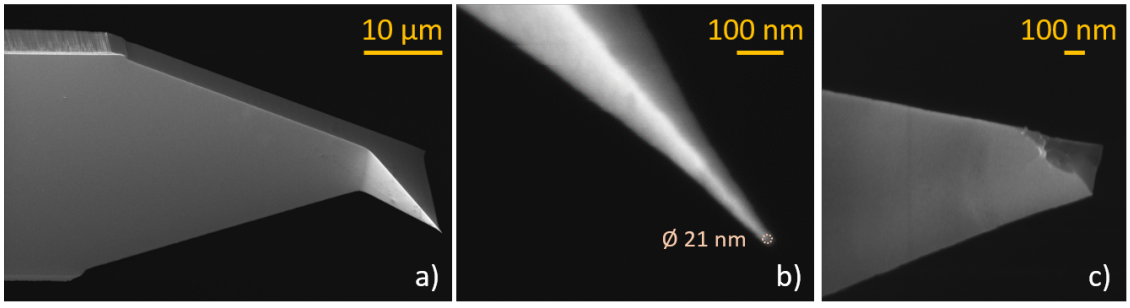

Figure 3.3: Asylum AC160TS-R3 AFM tip picture, a) and b) show respectively low and high mag of a new tip (picture taken at 45° stage tilt). c) shows the tip after being used for imaging the T657C3 sample (picture taken at 33° stage tilt)

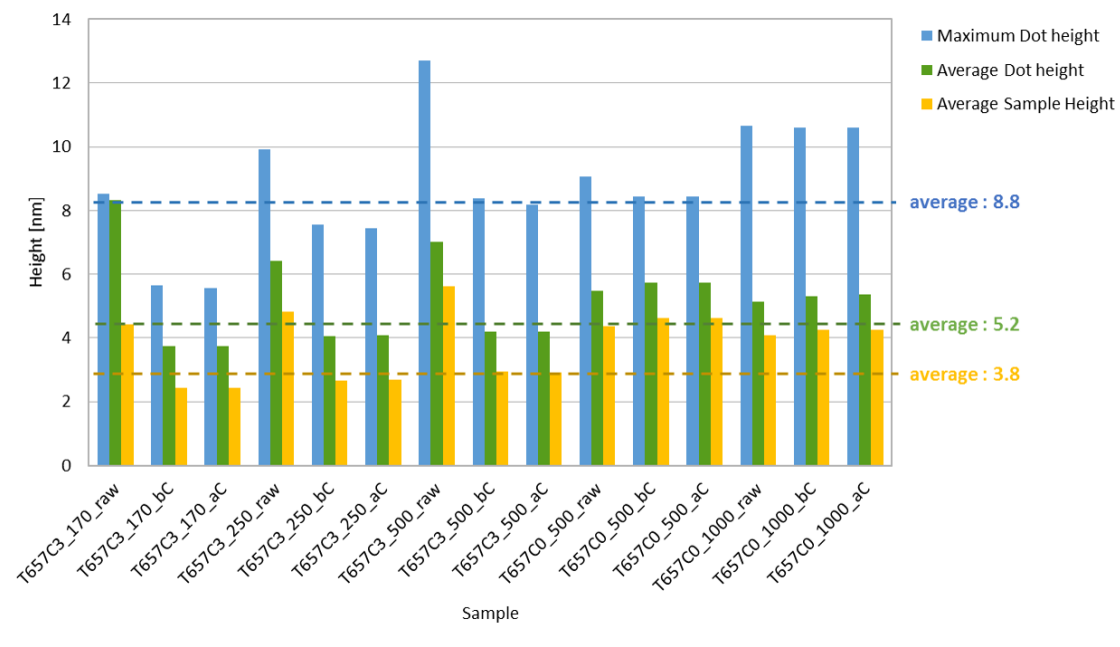

Figure 3.4: Maximum and average height from raw picture, before convolution and after convolution.

the image and then count the features remaining but the results were not good enough to be mention. This is why a short python script was written (based on mahotas [26]). The approach chosen was to try detecting the QDs by finding the local maximums in pictures. In this algorithm, two main parameters can be used; sigma and the disk size. Sigma is the amplitude of the Gaussian blur applied to the data that reduces the noise —allowing better counting. It was set to one by default although it seldom had to be decreased down to 0.3 for a big scanning area (1 micron square) or a high magnification picture (170x170 nm). The disk size is the size of the local maxima and helps avoid detecting multiple QD in one. The script is designed to find a good value automatically by pre-scanning the picture and trying to determine the average size of the profile. This auto-evaluating feature (applied when the disk size is set to 0) is hence dependent on the sigma parameter value.

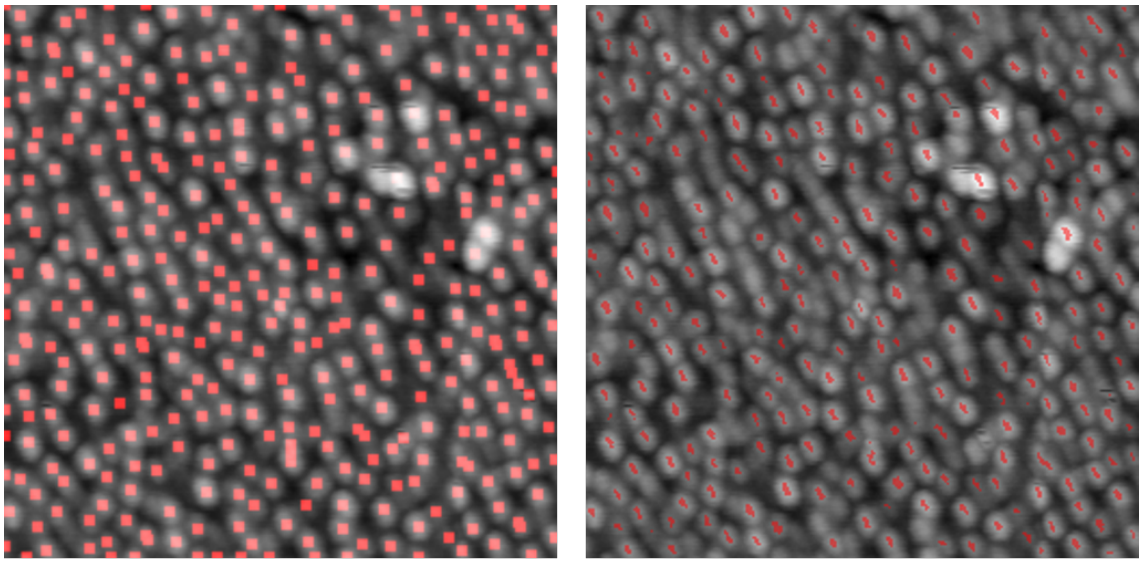

Figure 3.5: Number of dots found with the Python script and Gwiddion.

Figure 3.5 displays the output of Gwiddion watershed algorithm compared to the python script. By using an attentive eye or zooming in the picture, one can observe the python script detects more QDs and hence seems to provide better results.

Image Processing

Preliminary Verifications

The python script appeared to provide better results so far. It was decided to verify it and eventually rely on it for the rest of this study. The way the algorithm was checked was by competing against a human. To do so, several AFM pictures were used. Some of them were cropped to allow manual counting whereas other pictures with a higher magnitude were not. Two human were used, one that did not know how the software would run (referred as the unaware

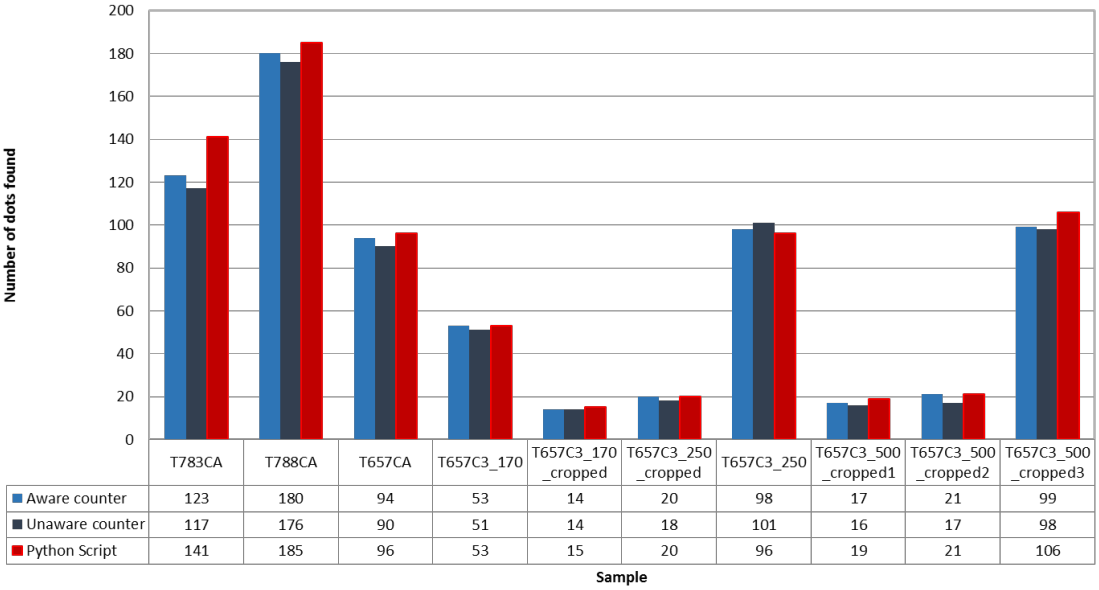

	T783CA	T788CA	T657CA	T657C3_170	T657C3_170 _cropped	T657C3_250 _cropped	T657C3_250	T657C3_500 _cropped1	T657C3_500 _cropped2	T657C3_500 _cropped3
Aware counter	123	180	94	53	14	20	98	17	21	99
Unaware counter	117	176	90	51	14	18	101	16	17	98
Python Script	141	185	96	53	15	20	96	19	21	106

Figure 3.6: Number of QDs found in the same picture according to the python script, a user that knows how the script works and one that does not.

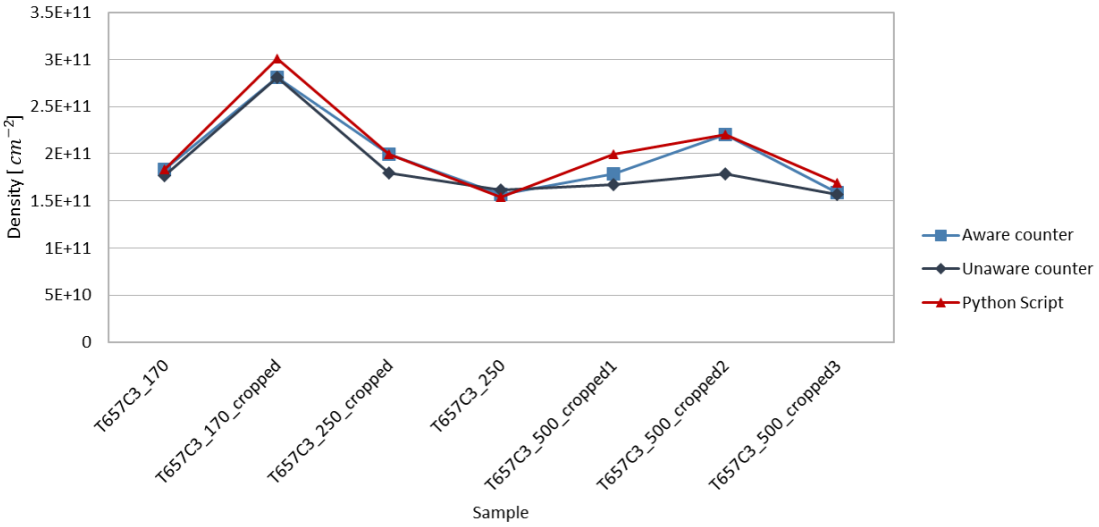

Figure 3.7: Density of T567 from several pictures and cleaves.

counter) and myself knowing what the script is looking for (referred as the aware counter). The result is displayed in figure 3.6. It appears that the result are quite consistent with an average difference of 4% (and going up to 14%) for the aware counter and 10% (with a maximum of 20%) for the other counter. The maximum error happened in both cases for sample T783C0. This can be explained by the fact that the algorithms tries to find regional maxima compared to a specific disk size. It is thus bound to this disk size and would perform badly if the sample had a large variety of QD sizes; this is the case in this sample where one can observe a larger distribution of QD diameters. By looking at all the pictures taken from the same sample and transforming the number of QDs counted into densities, one can observe the relative consistency of the measurement as presented in figure 3.7. The result was decided good enough to continue using the python script for the rest of this study. Furthermore, other feature were added to the script allowing one to evaluate other characteristics of the QDs such as the height, the radius of curvature and diameter.

Density

The density of the QDs was calculated using the python script. The results are displayed in figure 3.8. The results are different from what had been previously found and were thus verified by using multiple pictures. Since the raw data from Amethyst were not available, the python script ran on amplitude retrace provided in a PowerPoint.

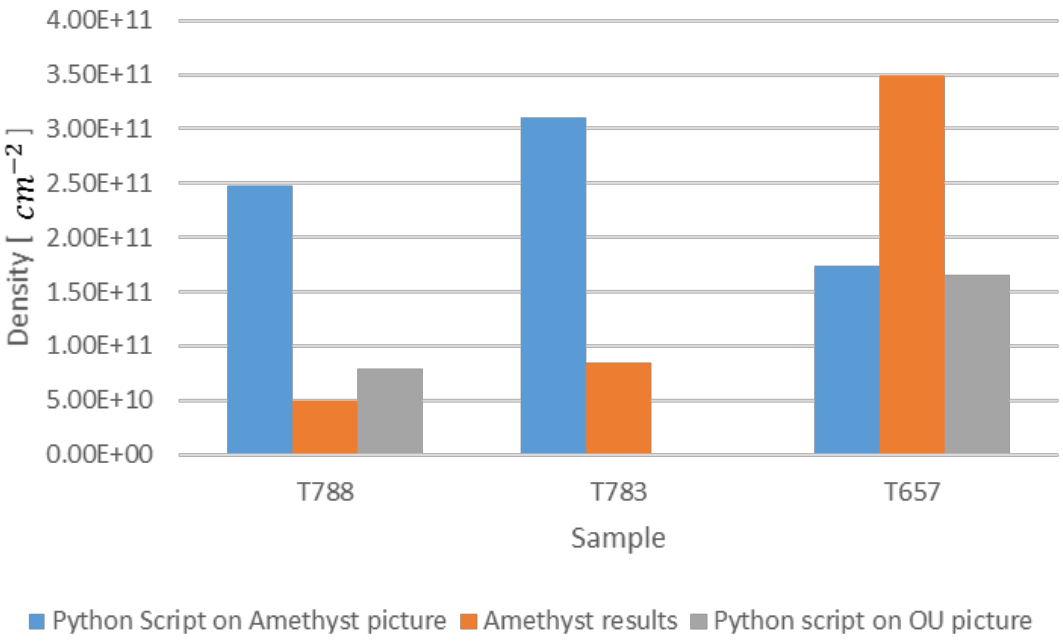

Figure 3.8: Density of T783 (0% Sn), T788 (7% Sn) and T657 (13% Sn).

Height and Radius of Curvature

After the number of QD was determined (and hence, their positions identified) information about the height and the radius of curvature could be collected. The height is a simple measure of the pixel colour at the QD position whereas the radius of curvature was calculated using the equation:

$$R = \sqrt{r_h \times r_v} \tag{3.1}$$

Where r_h and r_v are the radius of curvature on the horizontal and vertical axes. They were calculated using the mathematical formula.

$$r_{h,v} = \frac{(1 + y\prime^2)^{\frac{2}{3}}}{y\prime\prime} \tag{3.2}$$

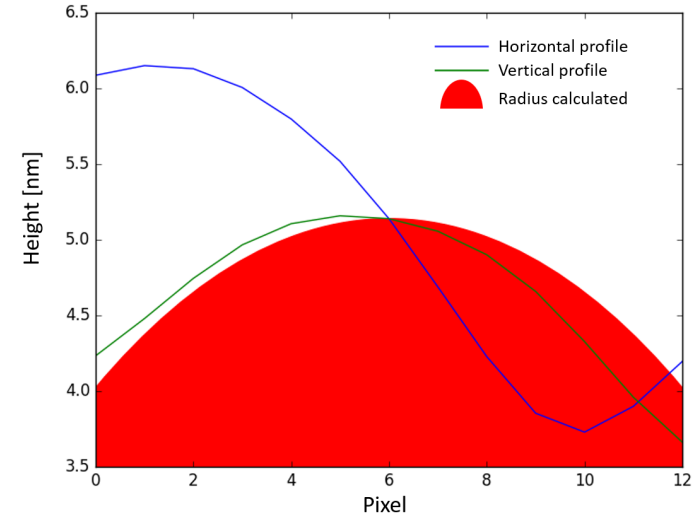

Figure 3.9: Horizontal and vertical profile within a QD disk size. Pixel 6 is the positions of the local maximum detected. The calculated radius is displayed.

Since the position detected is the centre of a regional maximum, it is not necessarily the highest position of the QD; the highest point can be anywhere withing this disk defined by the disk size parameter. Moreover, the position of the QDs are detected in a copy of the image, obscured by a Gaussian blur, while the the data are retrieved from the original picture. Figure 3.9 illustrates this statement. Because of that, the QD height calculated can be slightly off and so can be the radius of curvature. In our case, since a small disk size was used, it can be assumed that the calculated values are very close from the actual data. Figure 3.10 displays the height distribution of sample T783 and T657 whereas figure 3.11 displays the radius of curvature for both samples. Sample T783 has a larger height distribution while T657 is more uniform. Additionally, sample T657 has the highest height. The same trend can be observe in the radius of curvature distribution —T657 presents a narrower distribution. However T657 shows a radius of curvature mainly between ten and fifteen nanometres,

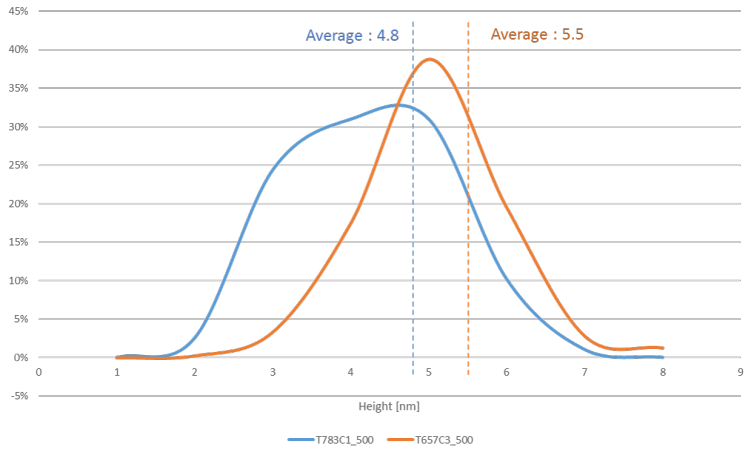

Figure 3.10: Height distribution for samples T783 (0% Sb) and T657 (13% Sb) samples.

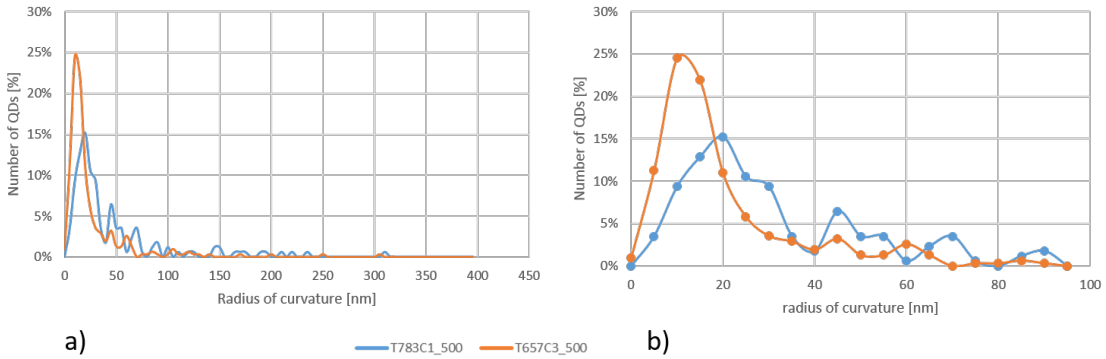

Figure 3.11: a) the radius of curvature distribution for T783 (0% Sb) and T657 (13% Sb). b) the beginning of the distribution displaying respectively 78% and 86% of the QDs

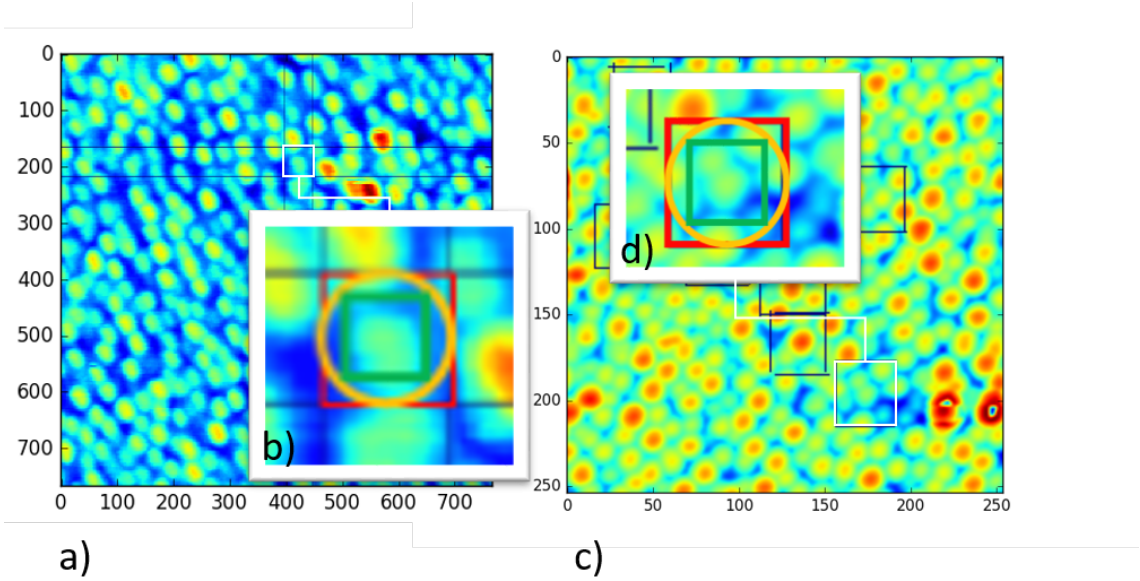

Figure 3.12: Figures a) and c) displays a QD border detected for a case where it works relatively well and one where it does not. Figures b) and d) are zoomed in version showing in red the area detected and in green the area considered.

suggesting the AFM tip is imaged rather than the sample's radius.

Diameter

Attempts to calculate the QD diameters were made. The Mahotas built in edge detection function (canny edge detection) did not provide a good result. In order to save time and for the first attempt, a simple 2×One dimensional (1D) approach was used; it detects when the local vertical and horizontal profiles reach a minimum. This provides four points that can be interpreted as a rectangle or an ellipse. The ellipse was chosen because QDs seemed to have an elliptic shape. The detected area with this algorithm was often considerably larger than the actual QDs. For a different consideration —including the theoretical shape of the dot (see subsection 3.3.4)— it was decided to reduce the area detected by taking the best fit for the inscribed square of the ellipse. Figure 3.12 displays

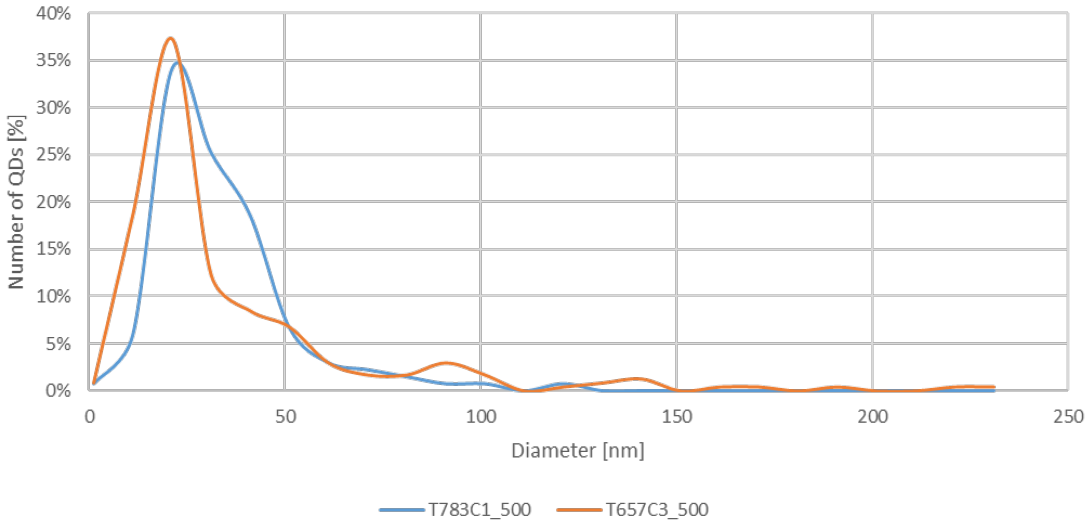

Figure 3.13: Complete diameter distribution.

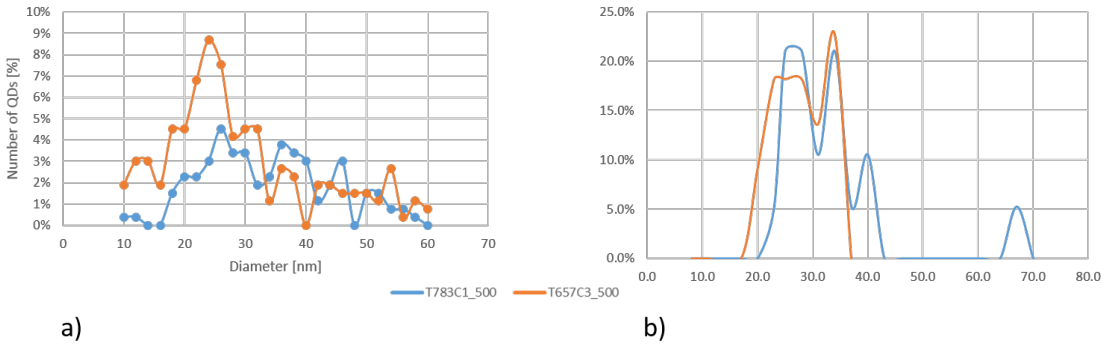

Figure 3.14: Diameter distribution with values between 1 and 60 nm. a) the result from the python script b) measured by hand

the detected rectangle/ellipse and the inscribed square we used, illustrating the detection steps.

This method was not highly reliable and probably provides better results for high density samples. Nonetheless the distribution of the diameters for samples T783 and T651 are displayed in Figure 3.13. Most of the diameters are under 60 nanometres which still seems quite high by looking at the pictures; Figure 3.14 highlights this region and compare it to manual data calculated on a small fraction of the picture (19 and 22 values for respectively T783 and T567). The automatic and manual result do not look similar although one can qualitatively notice the same behaviours; a narrower distribution for T657 and three peaks for T783. Once again sample T657 seems to have a better homogeneity with a narrower distribution. Indeed, in the automatic case, 42% of the T657 QDs have a diameter between 20 and 34 nanometres while only 23% of the T783 QDs are in this range. Sample T783 seems to have severall dot diameters in both automatic and manual cases, featuring QDs diameters around 26, 40 and 70 nanometres.

Size of the Wetting Layer

Estimating the size of the wetting layer seems possible with AFM data. To do so, two methods were applied :

- Matching pyramid method : the average characteristic of the QDs (height and diameter) are calculated and used to model an ideal sample where all the QDs are similar. The shape of the QDs was chosen to be a pyramid. Indeed, it has been shown theoretically and experimentally that InAs QDs have a pyramidal shape [21]. The volume per area of all these dots is then

Sample	Height $[nm]$	Diameter $[nm]$	Density $[cm^{-2}]$	Wetting layer size $[ML]$
T783C1–500	4	37	7.84×10^{10}	1.8
T657C3–500	5	30	1.55×10^{11}	1.1

Table 3.1: Wetting layer estimation using the matching pyramid method.

subtracted from the volume per area deposited on the sample, theoretically providing the height of the wetting layer.

- Mean value method : The probe is assumed to touch once the wetting layer (being the lower height; 0). The average height of all the scanned area is then a measure of the volume per area of the QD. Subtracting this number from the volume per area deposited on the sample provides an estimation of the wetting layer height.

The results of the matching pyramid methods are display in table 3.1. It was chosen to use the average of the middle of the distribution for the height data. The diameter was also chosen according to this criterion, but also taking into account manual data. The wetting layer calculated is 1.1 ML and 1.8 ML for T783 and T657 respectively. For sample T783, this is not far from the 1.6 ML measured from the reflection high-energy electron diffraction (RHEED) pattern, but only one diameter was assumed while it was found that the sample had a large distribution of diameters. The result of the mean value method was expected to provide better results since there are fewer assumptions; however, it is highly dependent of our assumption that the wetting layer is touch one, at the lowest point. As it turns out, this assumption must be wrong since the average height calculated for T783 and T657 (respectively 3.75 and 2.93 nm) is greater than the matter deposited (3ML, so about 0.9 nm). This of course leads to a wrong result with a negative wetting layer height. One could try to enhance

this result by calculating the average height of the QDs, and the average height of the area that is not considered as containing QDs and subtract them.

Chapter 4

Scanning Electron Microscopy

After analysing the AFM data, doubts arose regarding the accuracy of the measurements due to tip artifacts. This lead to the use of the Zeiss Neon 40, OU's' best SEM. SEM cannot provide 3D information like AFM does, but the two dimensional (2D) pictures can be taken at a tilt so that height information can be measured. This chapter relates the work done with the SEM machine.

Imaging Concerns

Several parameters can alter the SEM picture quality. Some of them can be easily modified by changing a value in the software, but others such as the beam coherence or the type of atoms present in the chamber are more difficult to change. This section covers the work done in order to enhance the picture quality.

Imaging Parameters

First of all, let's discuss about theoretical considerations regarding the SEM parameters. The features to image are very small —in the nanometre scale. In order to obtain accurate measurements of topological information, only secondary electrons (SE) (and preferably SE-I type [SE exiting the sample close to the beam]) should be used. This can be achieved by using the "İnlen" detector which is located in the objective lens and only captures SE. This can be done because the magnetic field that drags electrons back in the lens is too weak to affect back scattered electrons. Additionally, a small accelerating voltage must be use in order limit the size of the interaction volume. However, decreasing the acceleration voltage also limits the maximum theoretical resolution as stated by Abbe's equation.

$$d_0 = \frac{0.612\lambda}{n \sin \alpha} = \frac{0.753}{\alpha\sqrt{v}} \tag{4.1}$$

Furthermore, such a decrease also induces a diminution of the signal to noise ratio, ratio that can be improved by setting the smallest working distance (WD) possible. Smaller probe current can also helps achieve better resolution. However, the only way to control the probe current in the Zeiss Neon, is to modify the aperture size. Doing so also changes our α angle and could not result in a benefit.

Finding the Best Accelerating Voltage

To find the best accelerating voltage, several images were taken at 200 kX. The result is shown in figure 4.1. One can observe that 2 kV is too sensitive to contamination, preventing a good use of the dynamic range. The picture is also

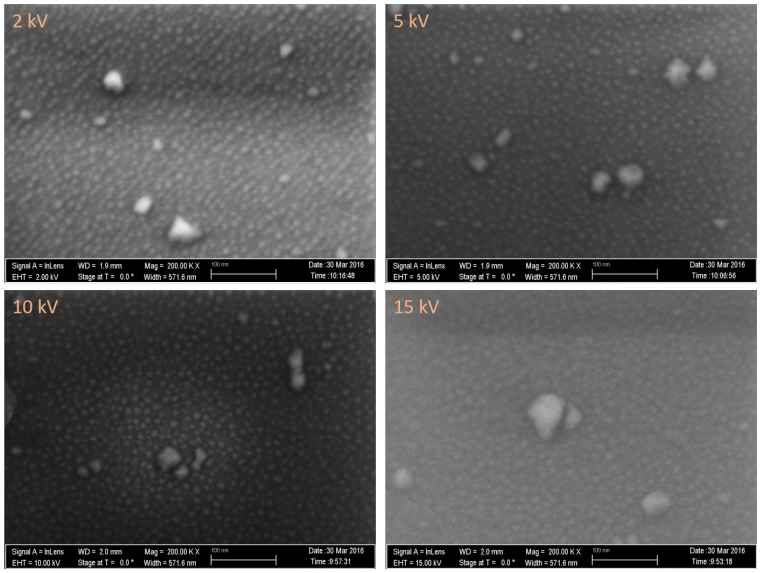

Figure 4.1: Voltage impact on the picture quality. Pictures are taken at 2, 5, 10 and 15 kV.

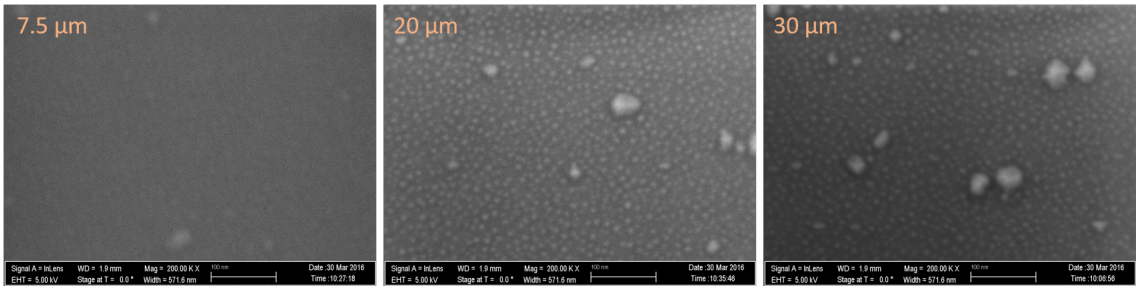

Figure 4.2: Aperture impact on the picture quality. Picture are taken with a 7.5, 20 and 30 μm aperture.

quite noisy. The 15 kV picture on the other hand, does not show clear QD edges and is also noisy. The difference between 10 and 5 kV is not that clear in this picture, nevertheless, 5 kV was chosen to be as surface-sensitive as possible.

Finding the Best Aperture Size

Similarly, several pictures with an aperture size of 7.5, 20 and 30 (default aperture) micrometres where taken. Figure 4.2 displays them. The 7.5 μm aperture is clearly not optimal with poor signal-to-noise ratio. The difference between

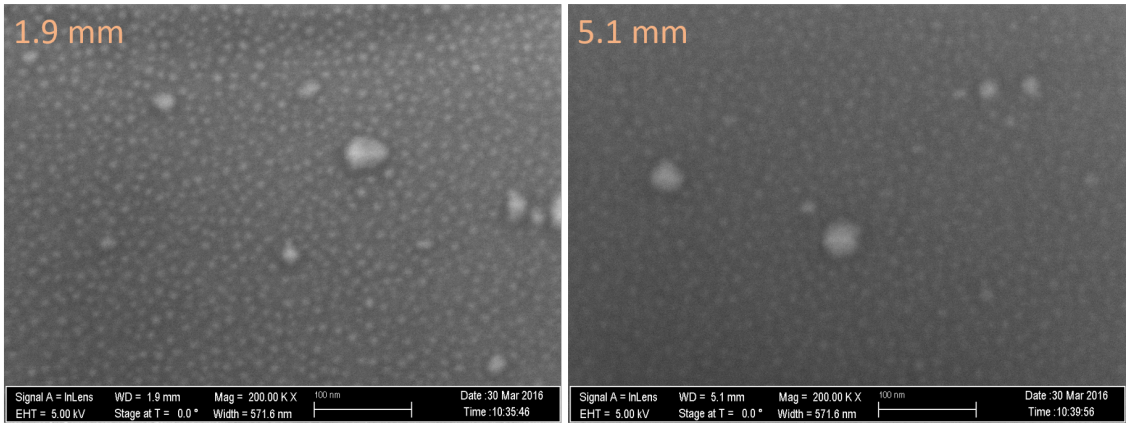

Figure 4.3: Working distance impact on the picture quality. Picture are taken with a 2 and 5 millimetres working distance.

the 20 and 30 μm apertures is arguable; 20 micrometres is generally more noisy but presents a better contrast. The thirty micrometres aperture was chosen because the additional noise that appears with the twenty micrometres aperture makes automatic image-processing harder.

Verifying the Influence of the Working Distance

Finally, a quick verification regarding the working distance (WD) was made. Figure 4.3 displays it; as expected, reducing the WD reduces the noise and provides a sharper picture.

Contamination Considerations

Even with the enhance parameters found in the previous section, the growth of carbonate contamination as much as the noise prevents taking good pictures. Additionally, it was found that the the QDs seemed to "grow" under the effect of the electron beam. The growth rate was not consistent and seemed to depend on the sample previously in the chamber. The growth rate was measure and is

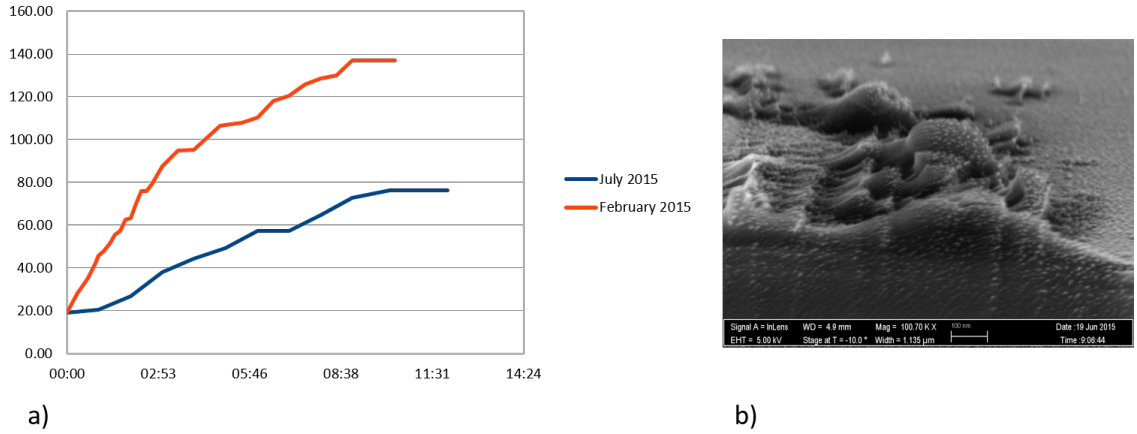

Figure 4.4: a) represent the average growth rate of the QDs. b) is the worse contamination that happened.

displayed in figure 4.4a. The orange curve displays the growth rate measured when the problem was discovered, while the blue curve was recorded after several cycles of in situ plasma cleaning for a total of about 13 hours. Doing so seemed to clean the chamber resulting in less contamination. However the growth rate was not consistent and depended on the samples previously put in the chamber. Hence, after imaging bio-films, a super-growth of hundreds of nanometres (c.f. figure 4.4b) was observed.

Those considerations suggested the need for cleaner samples and a cleaner chamber. A plasma cleaning of 8 minutes with 40 Watts was tested, without any notable change. In the literature, the National Institute of Standards and Technology (NIST) claimed to get rid of such contamination by overnight plasma cleaning [27]. It was decided to follow their recommendation.

An overnight –12 hours at 40W– O_2 in air plasma was done. It did not clean already-grown features such as those formed after imaging the bio-film. Nonetheless, the overnight plasma clearly improved the picture quality; the pictures where less noisy, sharper and less keen to contamination. However the

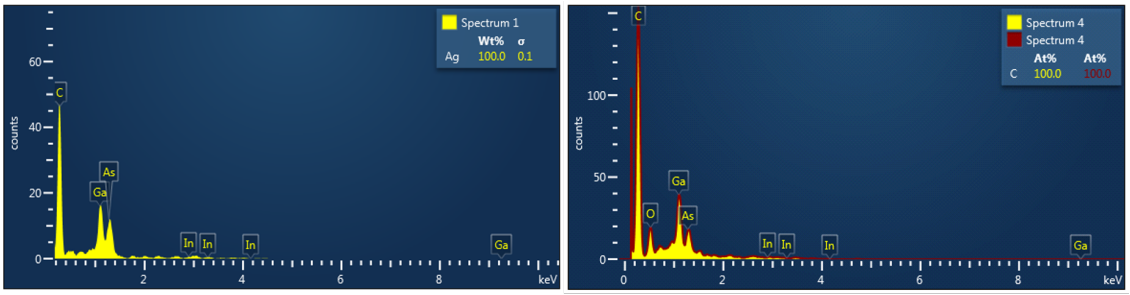

Figure 4.5: Comparison of sample composition, analysis by EDS, before and after an overnight plasma cleaning.

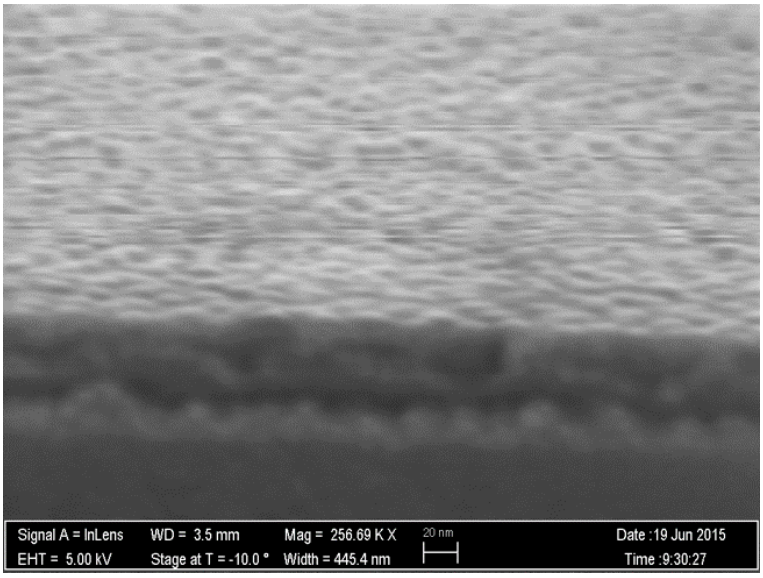

Figure 4.6: Image presenting the surging artifact.

overnight plasma was not totally beneficial. An energy-dispersive X-ray spectroscopy (EDS) analysis was done, showing the sample experienced oxidation ; figure 4.5 displays the result. Furthermore, the SEM stage was damaged by such long plasma exposure. The grease turned into a gummy texture preventing accurate movements and needing one to constantly reinitialise the stage position. Finally, an effect we named surging appeared. This describes a brutal movement of the stage that prevents good imaging (cf. Figure 4.6). Cleaning the stage helped reduce surging but to this day, the stage still present major

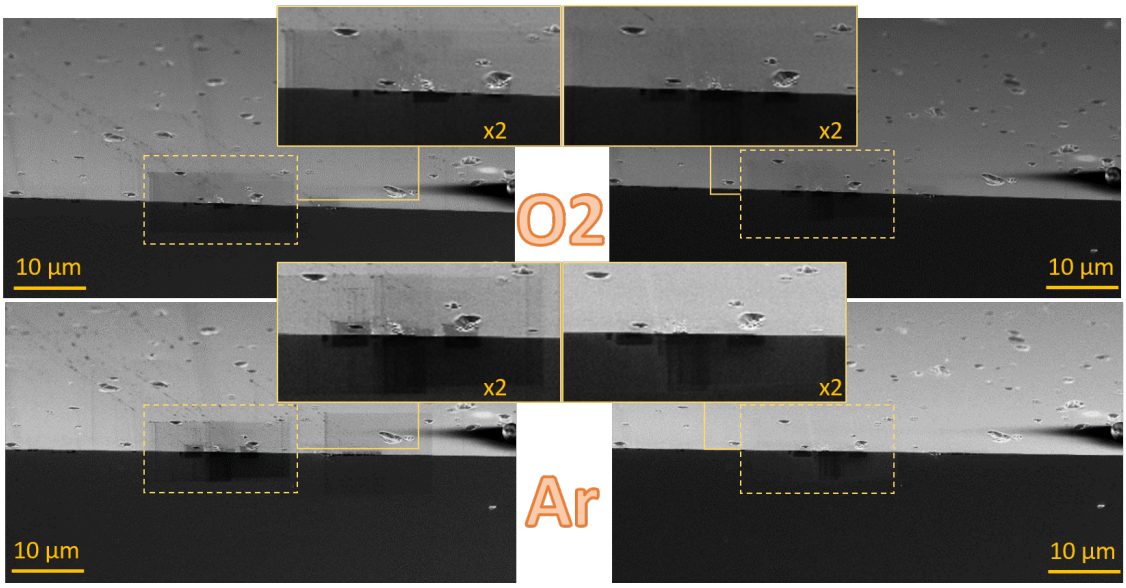

Figure 4.7: Comparison of O_2 in air and Ar plasma cleaning.

issues –especially when tilting. Because of the sample oxidation and the stage problem, it was decided to change the plasma gas and use a less agressive one —Ar. Ar was tested against O_2 in air. For the comparison, it was decided to zoom in several areas for a monitored amount of time (usually between 5 to 30 seconds) to take pictures. Figure 4.7 displays a low magnification picture of the same area before and after plasma-cleaning the sample for an hour at 40 Watts. As it turns out, Ar present a cleaner result than O_2. Indeed one can notice a slight carbon-layer contrast remaining after the O_2 in air cleaning while there is nothing remaining after the Ar cleaning. Ar should thus be preferred. However, because of the stage problem, it was decided to limit –if not stop– the use of in situ plasma until a solution for the stage is found.

The NIST claimed to be able to get rid of vibration efffect using software (ACCORD) [28]. Even though our "surging" effect was different than normal vibration it was decided to test if this software could improve the image quality. The easiest way to use the ACCORD software is to record a video with :

- The shortest possible dwell time
- No averaging and integration
- No compression
- As few environmental perturbations as possible (no phone, no talking, etc.)

As it turns out, the ACCORD software was not able to improve the picture. In fact, the sudden movement was difficult to follow leading to a discontinuous picture.

Density

The SEM pictures were generally more noisy than the AFM pictures, needing a higher Gaussian blur to properly count the QDs. However, if the default setting (set to one for AFM) was set to three, it could not be used consistently and one needed to adjust it in order to have the best results. Furthermore, most pictures were taken in a dirty chamber environment, facing contamination, the stage still being damaged. This time, manual counting was not done but it was meticulously verified that QDs were not over- or under-counted. Additionally, the python script was slightly modified so that the possible stage tilt angle could be taken into account. The influence of the angle over the density value was recorded. In figure 4.8 several pictures at 200 kX were taken at different angles (0, 27, 45 and 80 °). The angle did slightly influence the measured density, but the values are still within the uncertainty range. However, one should be advised

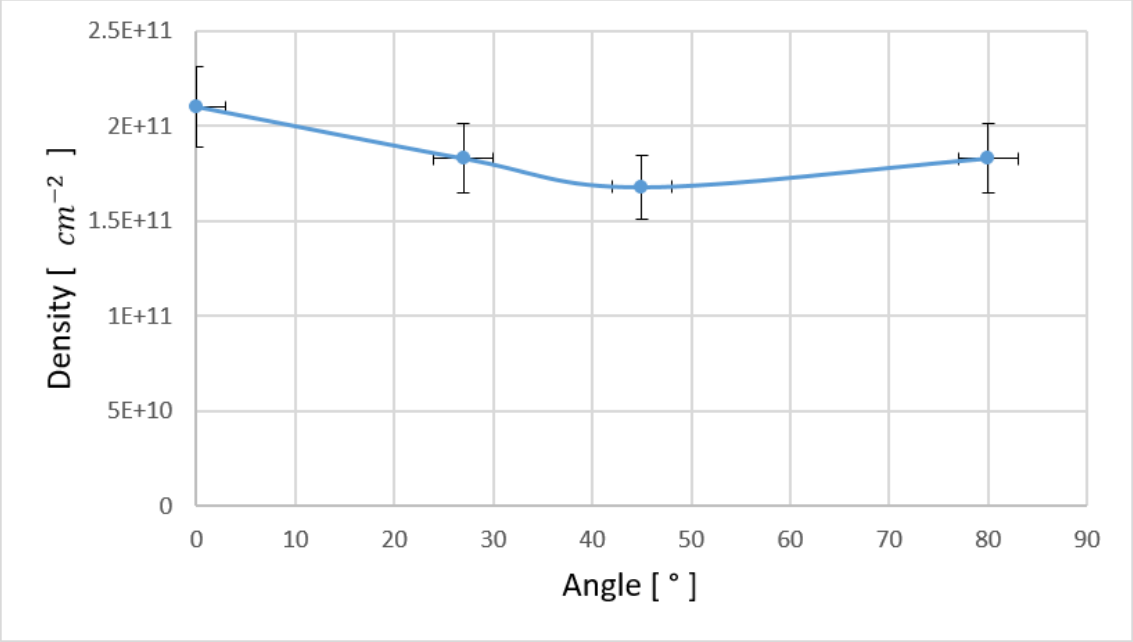

Figure 4.8: Plot recording the variation of the density with tilt angle.

to recorde density values systematically with an angle of 0 — theposition where the uncertainty of the angle is the smallest— for better density comparison.

Samples T783C0, T788C0 and T657C3 (respectively 0, 7 and 13% of Sb) were imaged in order to record their density. Figure 4.9 displays the density results. It can be seen that sample T783 has the lowest density showing the effectiveness of the strain releif compound. Sample T788 has a higher density than T657 with smaller QDs. This means that increasing the Sb concentration from 7% to 13% decreased the QD anti-coalescence effect.

Diameter

The AFM algorithm was used to determine the QDs diameters. It hence faces the same limitation regarding accuracy. Results are display in figure 4.10. One can observe than this result is not correct. By looking at the SEM pictures, it

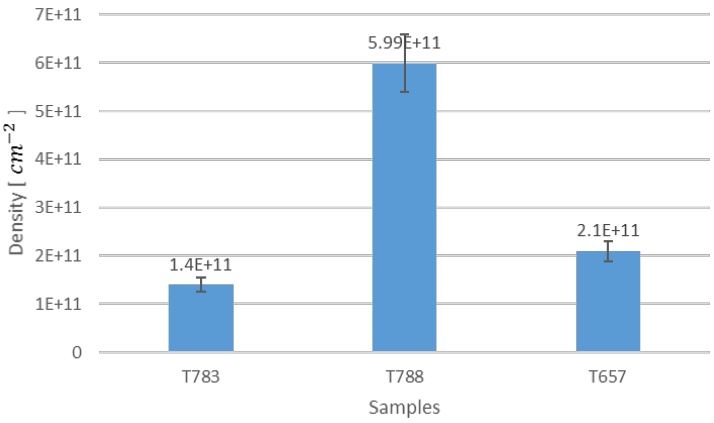

Figure 4.9: Density measured for several QDs samples.

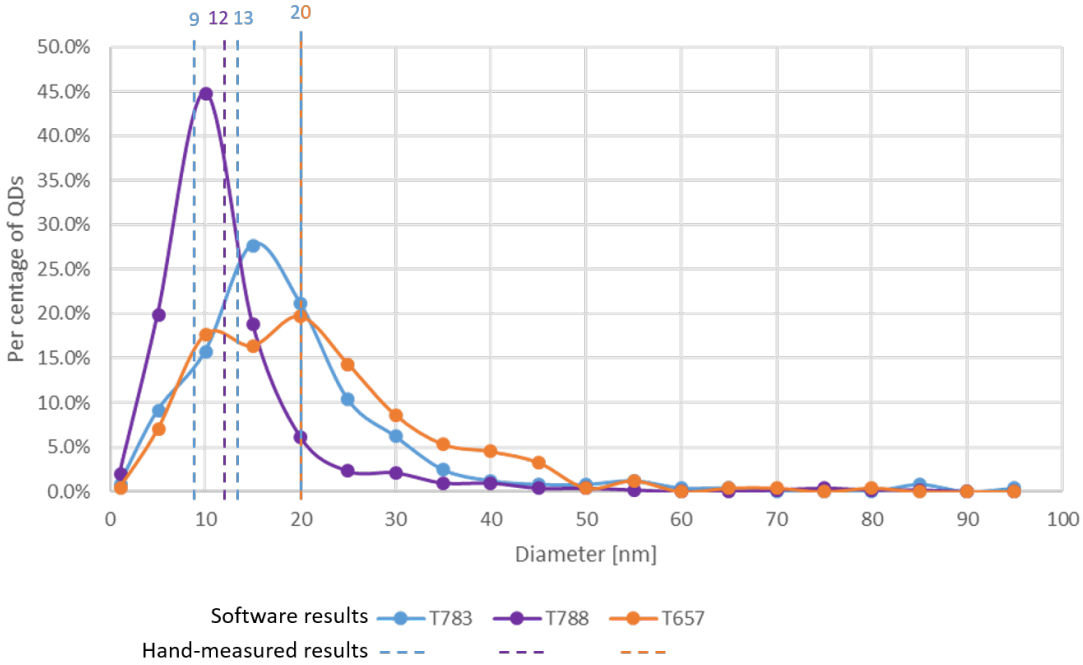

Figure 4.10: Diameter distribution for T783, T788 and T657. The average hand calculated diameter was added. Sample T783 presents two QDs size.

can been seen for instance that sample T783 possesses at least three QD sizes and should thus present three peaks. It was hand calculated that those peaks should be around 9, 13 and 20 nanometres, but there are also larger dots with a diameter up to 30 nanometres . This shows that one needs to think of an alternative method to efficiently calculate the QD diameters. For this reason, hand-calculated diameters were also provided for T788 and T657.

For sample T657, data extracted form cross-sectional measurements (for instance, measured in figures 4.6 and 4.13) were also analysed. It suggests a different, larger, diameter. Indeed, individual measurements or dividing the picture size by the number of QDs counted lead to an average QD size of about 26 nanometres.

Height and Radius of Curvature

As mentioned before, one can tilt the sample in order to determine QD heights. Angles around 90° must thus be used in order to have better results. However, the SEM cannot reach angles greater than 67°, needing one to mount the sample perpendicular to the electron gun. In order to do so, two holders were modified.

Specimen holder

The first holder is one of OU's classic cross-sectional holder. A clip was added so that the sample could be easily mounted and unmounted. Additionally a brass holder was modified so that it is able to convert a flat holder to a cross-sectional one and vice versa. The holders remain in the SEM lab and are available to

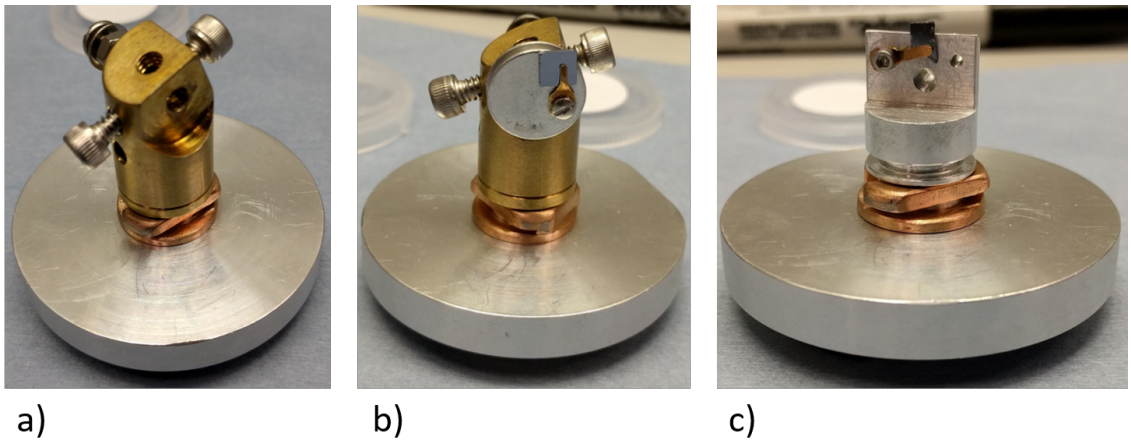

Figure 4.11: Flat / cross-sectional adaptor (a and b) and cross-sectional holder (c)

other users[1]; they are displayed in figure 4.11

Retrieving Height Data

Once the sample is properly mounted, an algorithm to record the heights was created. According to the image recorded, one can use the bright edge effect to detect the position height of a QD edge. By going forward in the x direction, one can thus record the height profile. However, this profile might not always be continuous. A correction was accomplised by adding another condition, if the recorded height is above the current one, instead of making a discontinuous connection, go a pixel higher and similarly for lower cases. Figure 4.12 presents the result of the algorithm on sample T657, with discontinuous and continuous detection. Once extracted, the trend-line of the profile was removed to correct the angle and a shift was applied so that the minimum value is zero. To calculate the height, it was decided to use the lowest point as zero and compare all local maximum heights compare to it. The extracted and corrected profile is displayed

[1] Ask Preston Larson

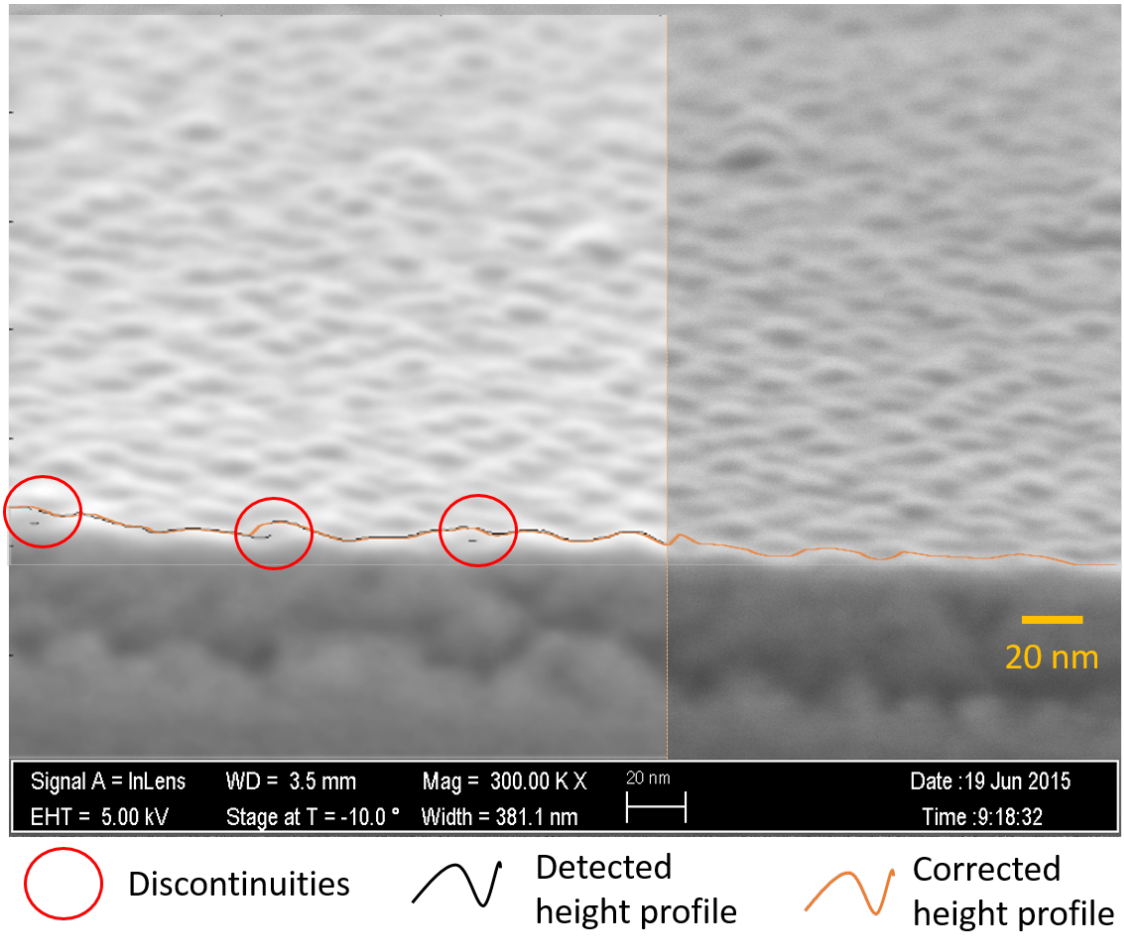

Figure 4.12: 80° T657 sample with edge-detection script output.

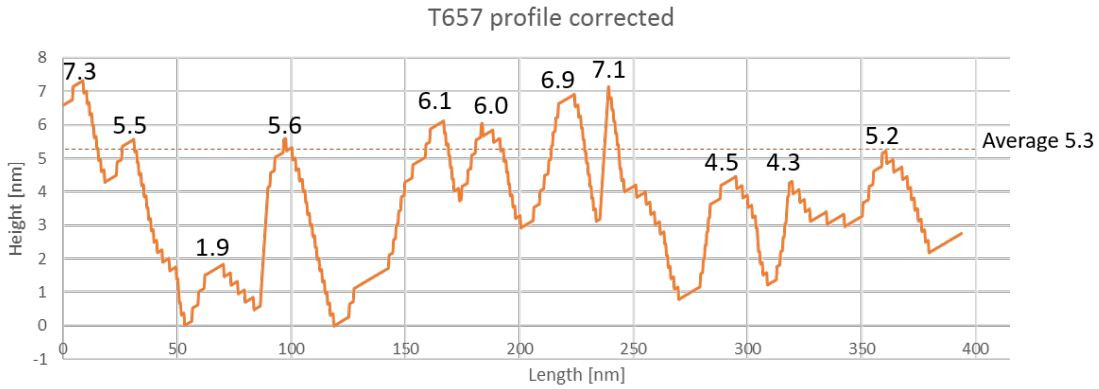

Figure 4.13: Height data exported and corrected.

in figure 4.13. The average QD height was find to be 5.36 nanometres.

The radius of curvature can now be calculated from this profile. However, a problem occurred. Indeed, the condition that the height profile must be continuous (which makes physical sense) implies that if you zoom in on each local maximum and evaluate the radius of curvature at this point, you will always find the same radius. This is because by definition, for a local maximum to exist, it must be higher that the two adjacent points. Since the points are discrete (pixels), the curvature at any local maximum is similar and defined by the pixel size. For this reason, a more complex algorithm is needed to calculate the best fitting shape for a certain height.

Imaging the Stacked Layer

Previously, only the top layer of QDs was investigated using AFM and SEM. However, it is well known that QD shapes change when a cap layer uis grown [29]. Additionally, stacked layers would be used in a final device and thus need to be characterised. This can be done by scanning tunnelling microscopy (STM) [30], TEM but a faster and easier technique would be very usefull. After several hours of plasma exposure, in a clean environment, the stacked layers of QDs seem to be visible. Figure 4.14 displays sample T657 with a scaled composition. Indeed, what looks like a stack layer of QDs is positioned where the layer should be. It was not done, but image processing can surely retrieve more detailed information tham what was manually calculated. The information retrieved manually is presented in figure 4.15. The staked QD's height —for sample T657— is about twice the height of the top-layer QDs. An average height of about 12.7 nm was recorded. To gather a more statistically significant

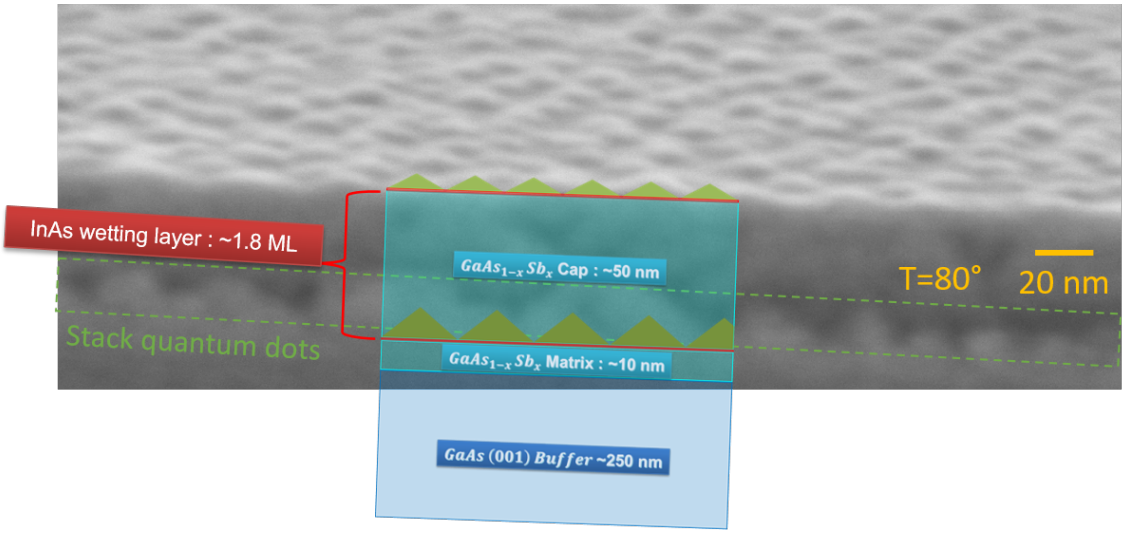

Figure 4.14: SEM picture showing a cross-section of T657 (with 80° tilt) and its scaled composition superimposed.

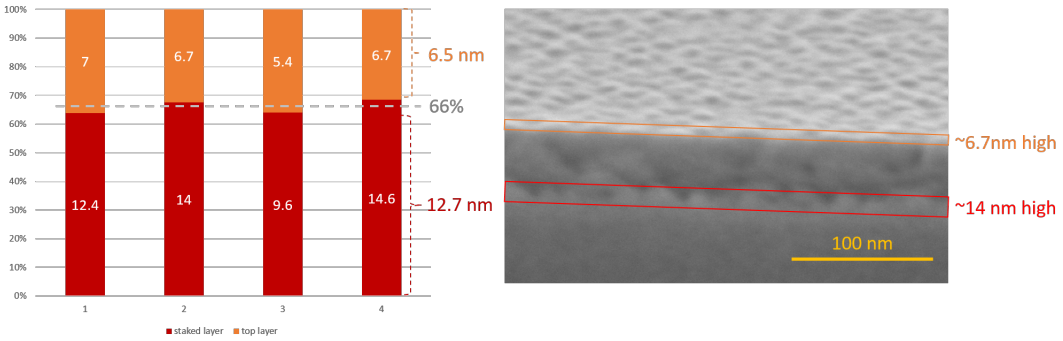

Figure 4.15: a) T657 QD top layer and stacked layer heights for four pictures. b) the measurements done on the 4^{th} picture

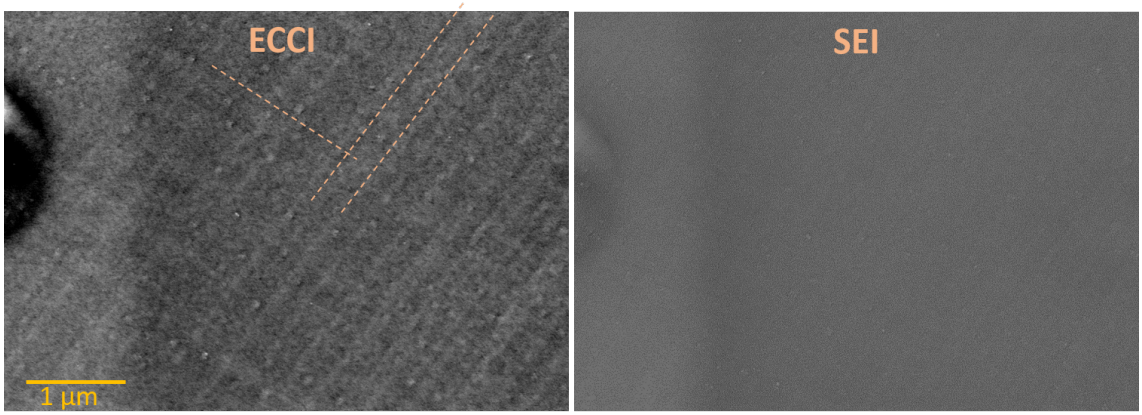

Figure 4.16: ECC vs SE at low magnification.

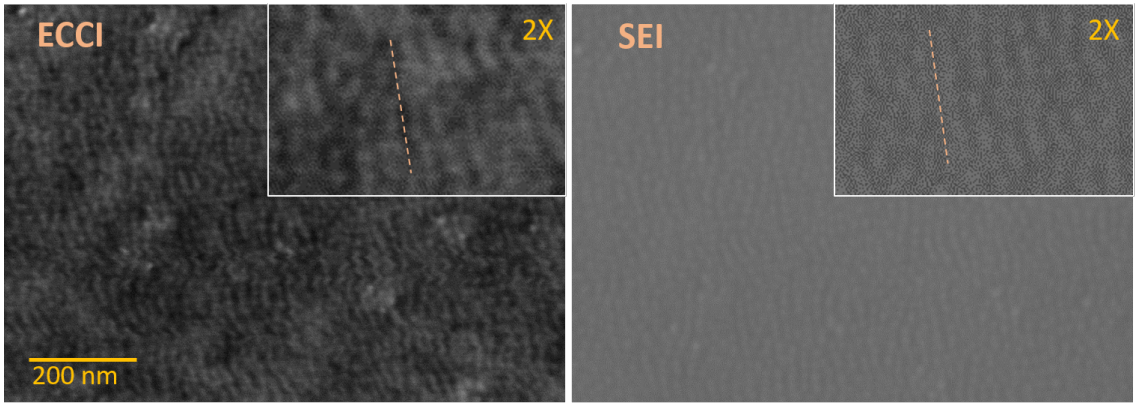

Figure 4.17: ECCI vs SEI at high magnification.

number of measurements, the FIB could in principle be used to etch the sample edge and image several lines of QDs.

Another Detector : Electron Channelling Contrast Imaging

In addition to the plasma cleaner, OU's SEM also possesses a solid state detector capable of providing electron channelling contrast imaging (ECCI). ECCI is very sensitive to topographic information as much as internal strain. Using ECCI

on T567 provided two new piece of information. The first one, presented in figure 4.16, is anisotropic cross hatching. Since ECCI is much more sensitive to strain than SE, the anisotropy is likely to result from the internal strain. The second one, presented in figure 4.17, is a clear image of QD chains.

Chapter 5

Transmission Electron Microscopy

TEM is ultimately the best and more reliable technique to observe the actual physical shape of our QD sample and thus determine if our AFM and SEM measurements are correct. However doing so is very time consuming and reducing the preparation time would be of great help. With OU's Zeiss Neon instrument, SEM and in situ TEM sample preparation can be done together, allowing one to select and prepare the area of interest he to image by TEM. This is a powerful tool that not only allows one to image a chosen area, but is also typically faster than traditional preparation techniques. However, this technique does require more training and monitoring without which, the preparation is likely to fail. In situ TEM preparation was enable when OU bought a Kleindink micromanipulator. However, since then, no samples were prepared and the methods had not been thoroughly acquired yet. This section documents our work in route to successful TEM sample preparation.

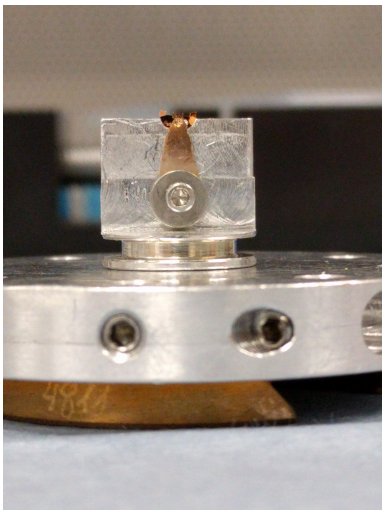

Figure 5.1: OU's TEM grid holder.

Sample Preparation

TEM Grid Holder

Even though making a TEM grid holder is separate from in situ site specific TEM sample preparation, it is a crucial step in the process and was thus should be mentioned. Grid holder can be bought online on specific electron microscopy site, however, they are rather expensive (about 1000 dollars [31]). It was then decided to build our own home-made grid holder. Stainless steal was first considered but rapidly changed to beryllium copper for additional stiffness. Figure 5.1 displays our grid holder; a small mark was added to create a more local pressure on the TEM grid. Omniprobe [31] grid were used.

Short Protocol

The protocol for doing is situ TEM liftout is well known and quite simple. A summarised version of this protocol can be find below and is illustrated in figure

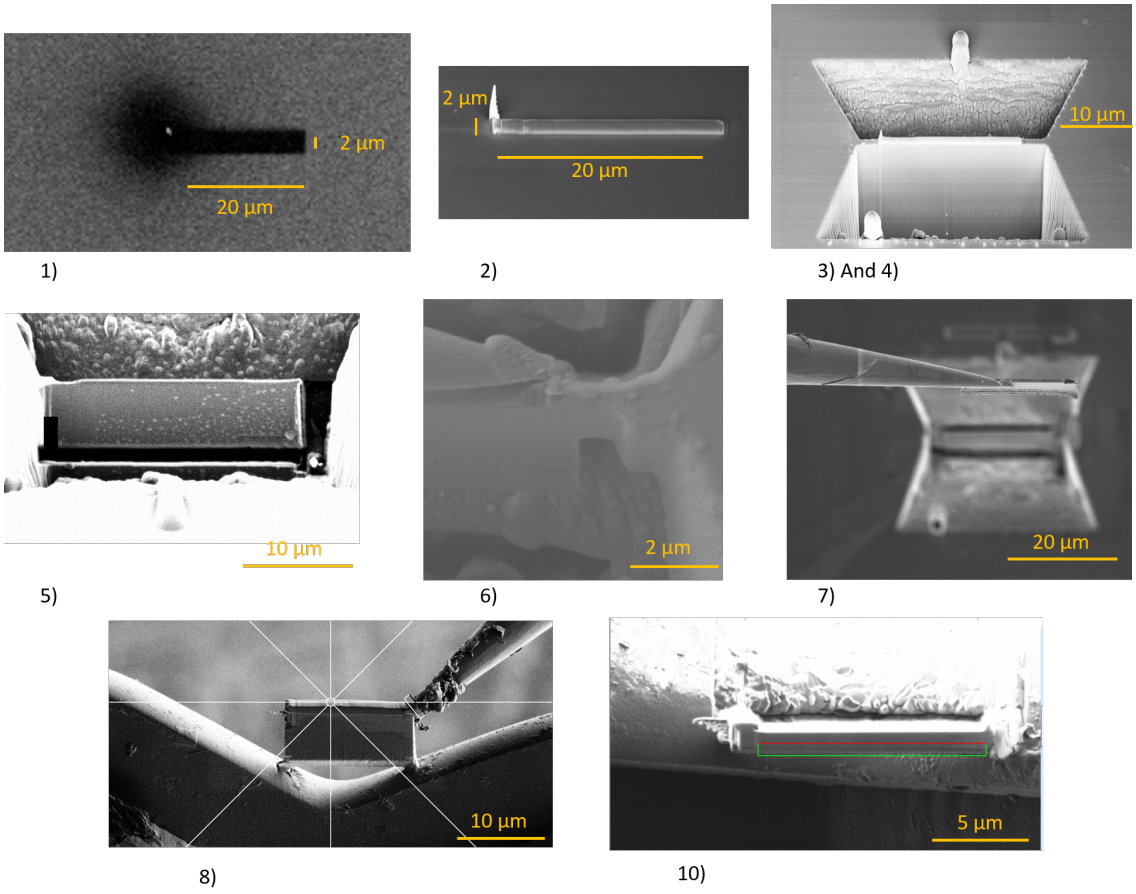

Figure 5.2: Short protocol for TEM sample preparation.

5.2.

0. Find the area of interest. This could be a particular defect or an area without defects.

1. Electron beam deposition of tungsten (W) on the selected area.

2. FIB deposition of W on the electron beam deposition layer.

3. Etch two coarse trenches around the FIB deposition.

4. Enhance the coarse trench by etching two smooth tilted rectangle areas.

5. Tilt the sample back to 7deg and etch one side, the bottom of the specimen and half of the other side, making a 'U' shape.

6. Spot weld the sample to the micro-manipulator.

7. Free the sample from the wafer.

8. Spot weld the sample to the TEM grid.

9. Free the sample from the micromanipulater.

10. Polish the sample.

Practical considerations and pitfalls make this process harder, needing additional technical details in order to perform this operation. This process was done and the new TEM lift-out procedure can now be found on the Zeiss Neon control computer[1]

[1]One can find it at the following path : "C:\Documents and Settings\All Users\Documents*TEM-LiftOut.pptx"

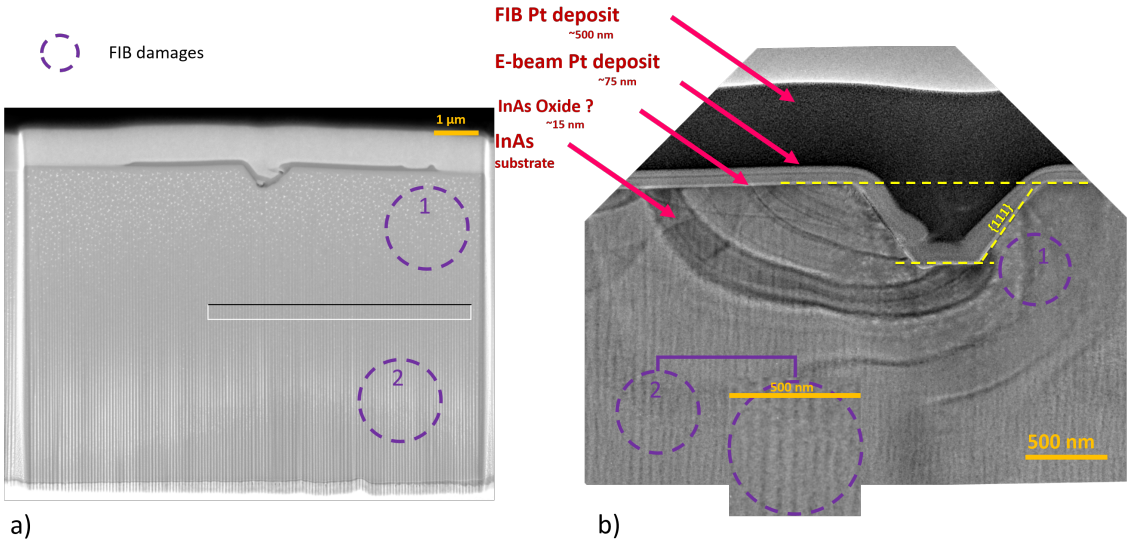

Figure 5.3: TEM low magnification pictures presenting two types of defects.

Sample Defects

Unfortunately, none of our attempts succeeded to make a TEM part. This is partially due to the learning curve of the process and mostly due to a malfunction in the Kleindink micromanipulator that has been sent back to Germany for repair. Meanwhile, the test sample that was done when the micromanipulator was bought to demonstrate its potential was studied. This was done because samples prepared with FIB are known to often present more damage —especially amorphization[32]. By imaging this sample with a JEOL JEM-2010 —a high resolution TEM— it was discovered that this technique introduced two types of damage.

The first one was mostly located at the top of the sample and looks like spotted damages. By zooming in, one can observe Moiré fringes, possibly indicating a polycrystalline material (Figure 5.4 a). Zooming even more allows one to observe lattices (Figure 5.4 b) with no obvious amorphization. This is confirmed by a

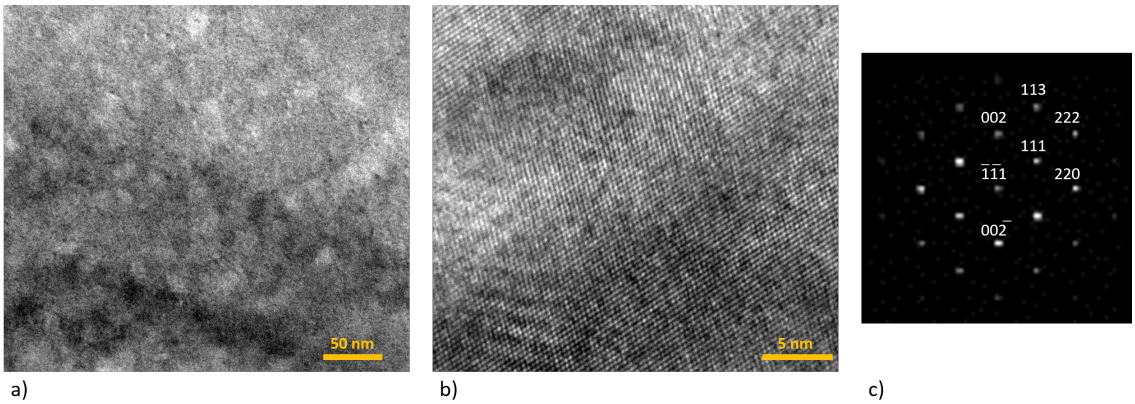

Figure 5.4: TEM high magnification pictures of the first defect: (a) the detect, (b) a zoom in version of (a) with the lattice visible and (c) the diffraction pattern.

bright field image of the area (Figure 5.4 c) that presents a clearly noncrystalline diffraction pattern.

The second defect was called "curtaining". Figure 5.3 shows that the curtaining effect is getting worse with depth. In Figure 5.3b, one can observe that the curtaining effect is present on the top of the surface; however, one cannot see it in Figure 5.3a until a certain depth, meaning the effect is getting worse with depth. Zooming in on it allows one to calculate the period of it, about 60 nanometres.

Surface damages can prevent achieving the best resolution and should thus be minimise. This was not done on this sample since it does not belong to our group, but several options could help to smooth the surface. If the same artifacts are seen on a future TEM liftout protocol, one should try (in order) :

1. Using different FIB parameters for the finial polishing

2. Using the low energy ion milling (GATAN). For an energy about 5 kV, damages are expected to be less than 3 nm [33].

3. Plasma etching.

4. Ozone or liquid etching.

Chapter 6

Discussion

As was previously mentioned, TEM could not be performed. Thus it is difficult to have clear answer regarding the shape of the QDs, and especially the stacked structures. Comparison between AFM and SEM data, knowing both limitations and artifacts, could nonetheless increase our understanding.

Density

AFM and SEM should be as capable when it comes to image density, however, one can see in Figure 6.2 that SEM indicates a higher density than AFM. The SEM density is 1.8 and 1.3 times greater than the AFM density for sample T783 and sample T657, respectively. One could question the quality of the QD detection, but it can be seen in Figure 6.1 that in both case the detection works well. This could be explained by the fact that AFM can be blind to small objects, and does not record the smallest QDs. SEM should theoretically be the most accurate; however depending on the chamber cleanliness, the noise can be quite high, preventing good detection. For sample T657, the best SEM

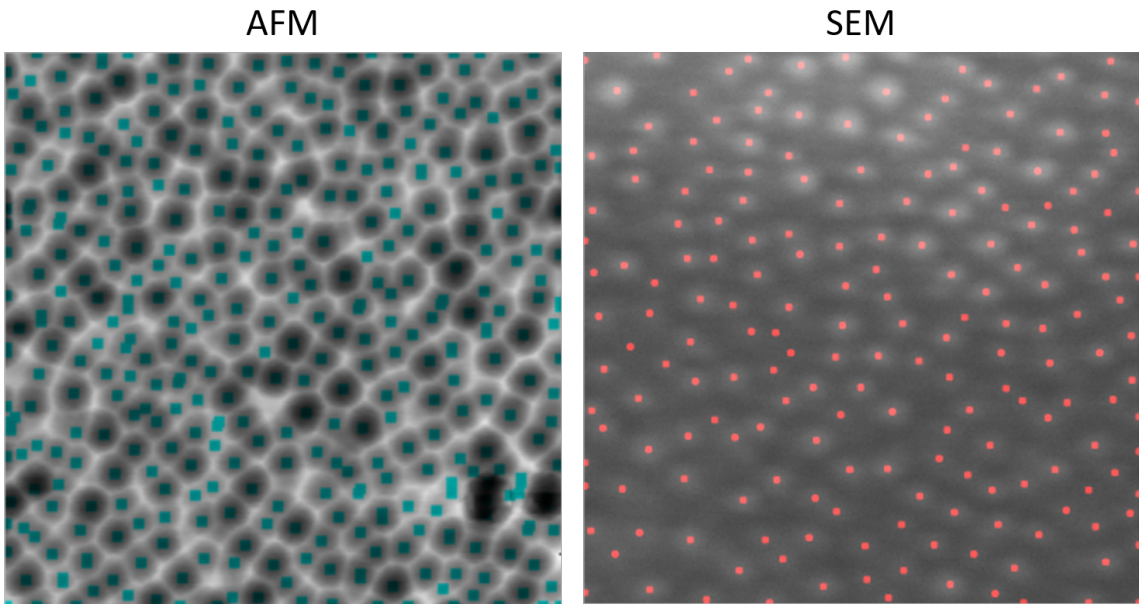

Figure 6.1: QD detection by AFM and SEM

Figure 6.2: QD density determined by AFM and SEM

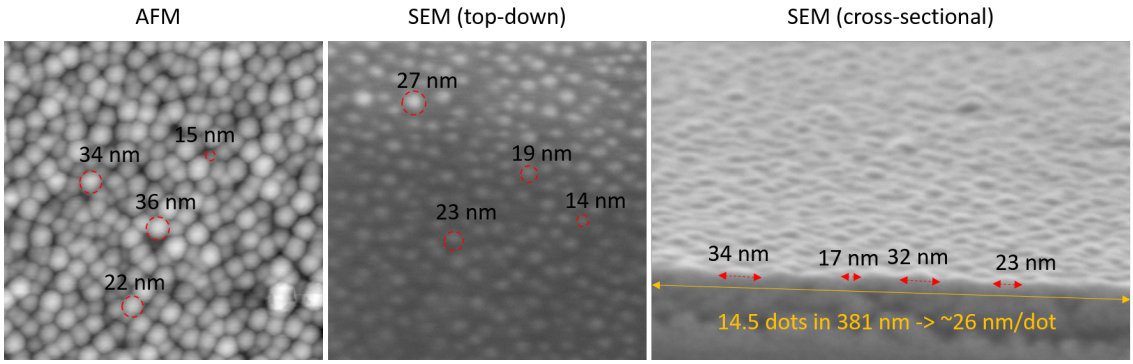

Figure 6.3: AFM and SEM pictures with some diameter highlighted.

picture provides a value of $2.1 \times 10^{11}\ cm^{-2}$, but the average SEM density was calculated to be $1.8 \times 10^{11}\ cm^{-2}$; the AFM picture provides a density arround $1.6 \times 10^{11}\ cm^{-2}$. The density of about $1.8 \times 10^{11}\ cm^{-2}$ is believed to be the most likely since it occurred a large number of times and places $1.6 \times 10^{11}\ cm^{-2}$ and $2.1 \times 10^{11}\ cm^{-2}$ at the limit of the assumed 10% error range. For sample T783, the AFM value (1.8×10^{11}) was chosen because of the noise level in the SEM picture, and the different QD sizes are prone to cause false detections. For sample T788, only SEM data was available, the pictures were clear with good detection; the value was kept.

Diameter

It was previously mentioned that a better way to automatically measure the QD's diameter needed to be found. In both cases, AFM and SEM, the result did not appear to be correct. Hand-calculation on the images provided by both microscopes do not agree (c.f. Figure 6.3). AFM presents wider QDs than SEM. Surprisingly, SEM plan view and cross-sectional results are not consistent, cross-sectional information being larger and closer to AFM values. This could

be because SEM is not height sensitive and SE from between QDs do not escape. This would lead to smaller QDs with larger separation regions which is what is observed. Additionally, the noisiness of the SEM images limits the ability to define where QDs edges are —especially for an algorithm. SEM cross-sectional images should provide the best data but with non-statistical numbers. In this case, for sample T657, the 26 nanometres given by the cross-sectional SEM picture was found to be plausible. For sample T783, it is harder to tell since the images obtain from both microscope are radically different. Additionally, the fact that the QD sizes vary widely suggests that a single number would not be the best way to describe the QD sizes.

Height and Radius of Curvature

The AFM and SEM height data could not be compared for T783 and T788 because cross-sectional SEM could not be performed for these samples. On sample T657, AFM provides data with a height around 5 nanometres whereas SEM provides data saying the height is about 5.3 nanometres. This is very close and likely to be correct. In both cases, one should wonder if the zero height, the reference point, is the surface of the wetting layer or any other point. With SEM cross-sectional images, one can simply measure on the sample that any dot has the recorded height and thus verify the result. On AFM, with a high density sample —and especially with a dull tip— the wetting layer is less likely to be reached, meaning the zero point is higher than it should be. For this reason, on high density samples like T788 and T657, SEM should be done in order to corroborate the AFM result. Concerning the stacked layer, only SEM could provide information, and just for sample T657, meaning there is noting

Sample	Height $[nm]$	Diameter $[nm]$	Density $[cm^{-2}]$	Wetting layer size $[ML]$
T657C3–500	5.3	25	1.8×10^{11}	1.36

Table 6.1: Wetting layer estimation using the matching pyramid method

to compare the data with. However, one must remember that this information was acquired with cross-sectional SEM in a clean environment and should ergo be correct.

The radius of curvature is probably the least correct information, at least at its current state. The radius of curvature was estimated by the radius of curvature of the local maximums. This seemed to be the easiest way to obtain such information, but the physical reason linked to the way data are acquired makes this number likely incorrect. Indeed, it was explained for the SEM case that the condition that the height profile must be continuous leads to similar radius of curvature measurements with the technique used. Amelioration could be done by finding the best fitting radius for a larger portion of the curve. The same effect can occur for AFM, and especially if the tip is being imaged, meaning the result should be read carefully. The fastest way to have an idea of the radius of curvature would be to measure it directly on cross-sectional SEM pictures.

Wetting Layer

With the information in the previous section in mind, the wetting layer calculation for sample T657 should be done again, taking into account the changes introduced by SEM measurements. The number obtained, displayed in Table 6.1, is closer to the RHEED measurement (1.7 ML) meaning the values are probably closer from the actual feature sizes.

Best sample

The previous data obtain from Amethyst's AFM suggested that sample T657 had the best density and shape uniformity. The results presented here however are contradictory and present T788 as a better candidate. Indeed its density is about three time greater than T675 and Figure 4.10 shows a narrower distribution of diameters, meaning the QD diameters are more homogeneous. Further measurements should be done to confirm this and obtain information regarding the QDs' height as much as their shapes in stacked layers. This could be done by cross-sectional SEM but the stage still presents issues. The micromanipulator should be back soon, opening the way to TEM.

Chapter 7

Conclusion

Developing third generation with low cost/watt is the final goal of the project. To do so, the IBQD design was chosen. Several set of InAs QDs on $GaAs_xSb_{1-x}$ were grown and needed to be characterise. Three samples with different Sb concentration were imaged with AFM and SEM in order to characterise them. TEM was also aimed, but developing the in situ TEM preparation protocol as much as the failure of the micro-manipulator delayed us. Generally, AFM was find to overestimate the size of the QDs as much as having a slightly lower density. On the other hand, SEM, and especially with preliminary in situ Ar plasma cleaning, was found to be more versatile. In fact, SEM was found to provide better density, diameter, height and radius of curvature as much as providing an idea of the staked layer height. Both machine provided about the same height information. The radius of curvature as much as the diameter was harder to calculate automatically and better algorithms must be written. Sample T657 was believed to have the best characteristic from previous measurements. However, the work related in this paper suggest sample T788 featuring 7% of Sb has the best density ($\sim 6 \times 10^{11}$) and the narrower size distribution. Further analyses

and especially TEM must be done to further understand the QDs's stack layer form.

Part II

Another FIB usage: 3D reconstruction

1. Introduction

Darwinian evolution has been a very successful theory that explains why Earth's species evolve. However, what causes these changes cannot be explained and must be studied.

Understanding biodiversity changes and the impact of environmental changes on biodiversity is a great challenge for many biologists. By understanding past events and the effects on biodiversity, paleobotanists hope to predict the impact of future changes such as ones introduced by humans (global warming, deforestation, change in ocean pH, etc.)

One of the major interests of paleobotanists is the downfall of the diversity among Lycopsids and the rise of diversity among ferns during the late Cretaceous period. Sorting species by their characteristics and recording which of those were present at what time provides insight into how species evolve and why some species are more diverse than others. The goal of this thesis part is to examine the inner exine (protective wall) porous structure of Arcellites hexapartitus megaspores. Doing so will help to understand the relationships between Arcellites species and others (mostly water ferns and Lycopsids) and possibly find characteristics that would categorise Arcellites. Furthermore, studying the inner exine porosity could help to understand the function of the channels during deposition of the wall and during the life of the spores.

2. Background Information

This paper is a M.S. thesis in the field of engineering physics. However, this part contains multiple references to biological terms, making it necessary to provide some background information and definitions. Additionally, information regarding the FIB geometry will be given.

Spores

Heterospory describes the production of two sex-differentiated spores. It is an evolution of homopory (or isopory) as part of the process of sex-differentiation in evolution. Heteroporous spores are composed of haploid cells protected by resistant walls. The male spore, called the microspore, is generally smaller while the female spore, called the megaspore, is generally larger. In fossil records, the gender of a spore can be ambiguous, which is why the size of the spore is often used to determine gender. It was proposed in the 1960s that any spore greater than 200 micrometre (μm) was a megaspore. For Arcellites hexapartitus, the main body was found to vary from 170-265 μm whilst in situ and attached microspores were found to have a diameter between 33-40 μm (see figure 2.1). The walls of the megaspores can be described in three layers, starting from the inside: the intine (often missing), the exine, and the perine. Figure 2.2 displays

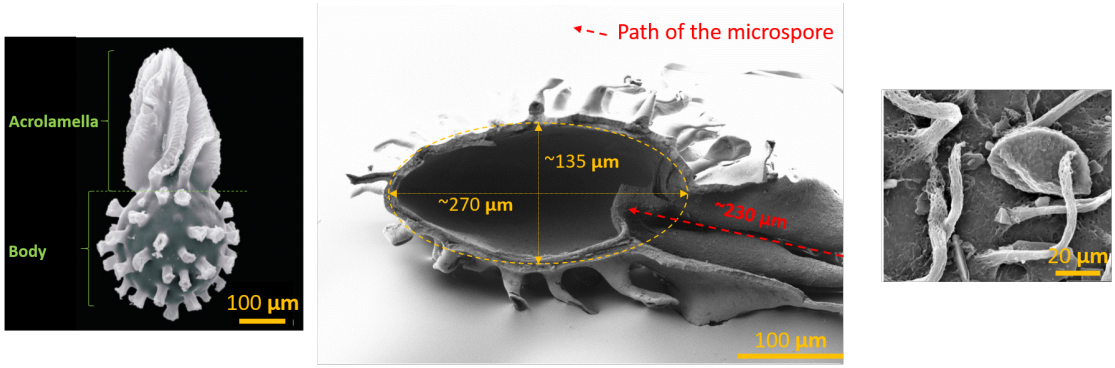

Figure 2.1: a) a full megaspore [6], b) a section of another sample and c) a microspore attached to a megaspore [6]

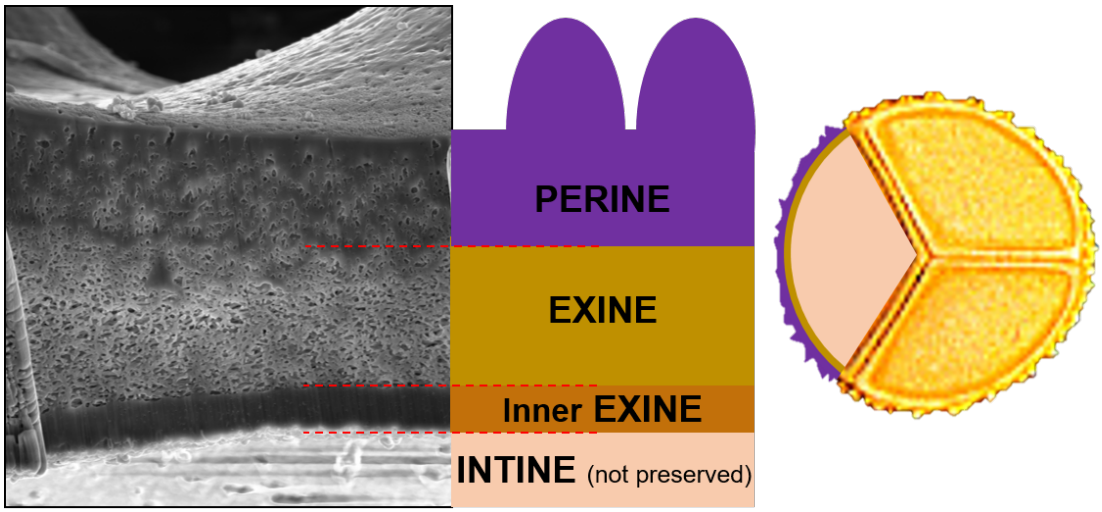

Figure 2.2: Megaspore's wall description

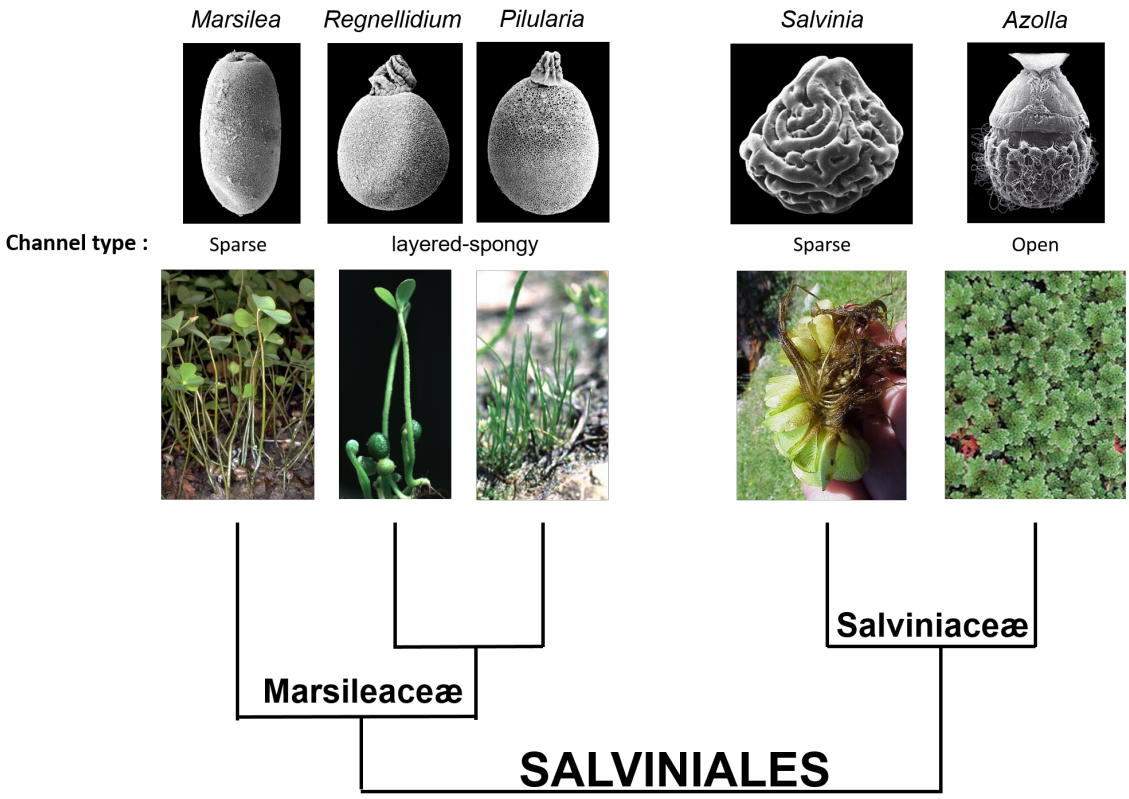

Figure 2.3: Marsileaceæ and Salviniaceæ families and their exine channel types (from [7, 8, 9])

the different walls composing megaspores; the left picture is a SEM picture of the studied sample. The inner exine is the focus of this paper. The inner exine is usually missing in broken specimens. Because of this, a megaspore with a full body is needed to examine the inner exine. The Arcellites hexapartitus megaspores found are not fossils in the sense that they are not composed of petrified organic matter. Instead, megaspore exines are composed of sporopollenin, a highly inert biological polymer.

Water Ferns

Arcellites species are believed to be descendants of plants that were located near or in water. This is why links with water ferns have been proposed.

Homoporous ferns produce sparsely channelled exines in most species. Heterosporous waterferns (in families of Marsileaceæ and Salviniaceæ) are different. Their exine channels can be sparse (Marsilea and Salvinia), layered spongy (Regnellidium and Pillularia), or extremely open (Azolla), as shown in figure 2.3. Betten et al. [34] used TEM to analyze Arcellites species. They found that most Arcellites are densely channelled. These channels were found to be perpendicular to the surface in most cases. This difference questions the relationship between Arcellites species and water ferns. This also suggests that Arcellites might be related to lycopsids [34].

This is why analysing the porous structure of the inner exine using FIB was investigated.

Project

Traditionally, megaspore species are identified through two electron pictures — a rough cross-section observed via SEM and a smooth one imaged with TEM (c.f. top pictures of Figure 2.4). The goal of this project is to demonstrate the potential of SEM paired with FIB to obtain similar results and investigate the porous structure of the inner exine (c.f. bottom pictures of Figure 2.4).

The specimens were furnished by Dr. Lupia from OU's Sam Noble Museum. Bonding specimens for SEM viewing and FIB slicing is a crucial non-trivial step.

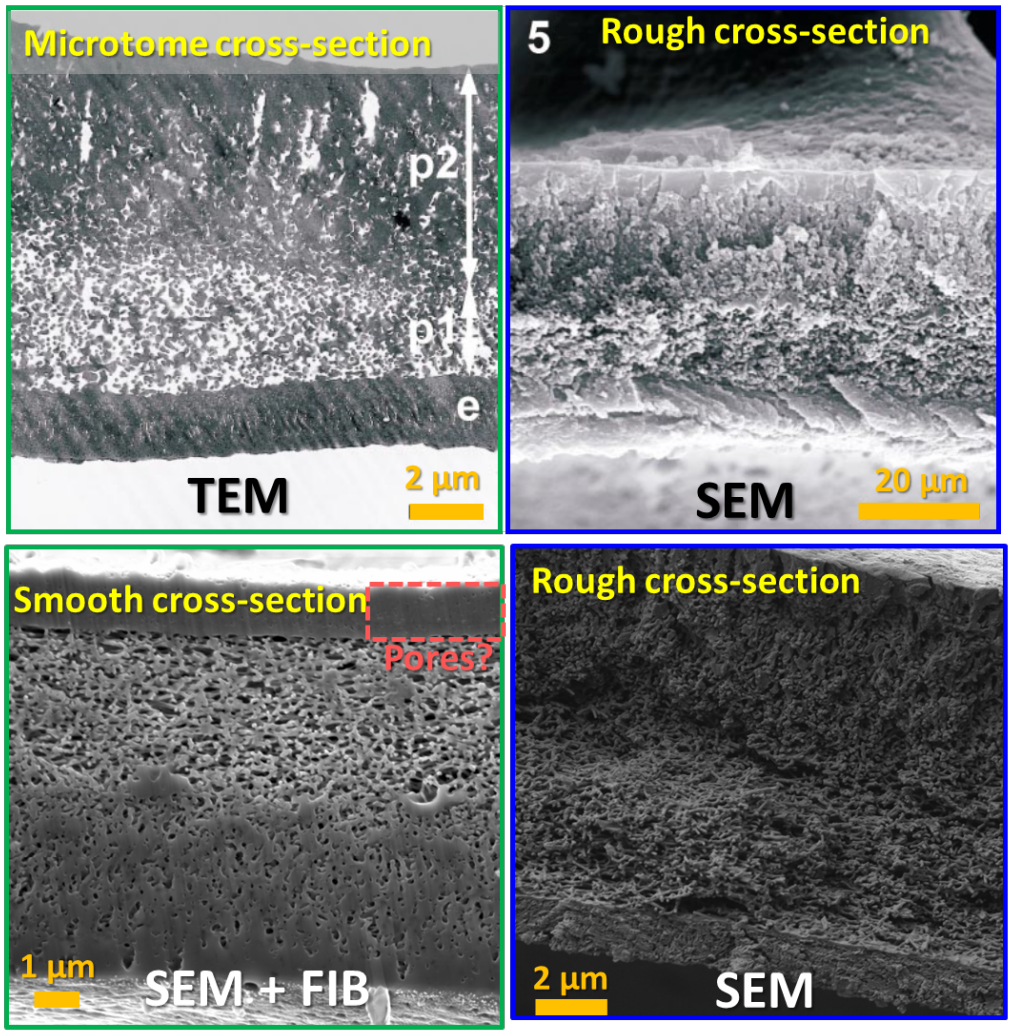

Figure 2.4: Top pictures are traditional images used to identify megaspore species; the bottom images are the alternatives investigated in this thesis.

We need to control the specimen orientation and coat to make conducting, this is not easy for samples that are 100 um in size. The old method involves B72 an acrylic resin (removable in acetone) and thick PdAu sputter coated layers. Generally Lupia maneuvers the specimen using a eye-lash on rod manipulator under a stereo zoom microscope. He is very adept at this procedure and can usually place the specimen in the B72 with the appropriate surface(s) showing without the B72 wicking over these surfaces. Although this is not easy. We switched to thinner sputter coated iridium layers, these worked except the iridium layer may introduce strain to the specimens and because the specimens are brittle this may cause the specimens to crack and even break apart. We stuck with iridiumidium coating and we tried to adjust the coating geometry to evenly coat all sides of a specimen equally. Even so we still had recurring problems with specimen cracking and breakage leading to the loss of parts of our specimens. We also moved away from B72 which wicks and can inadvertently coat the critical surface that should remain bare and dries too fast. We also decided to not use the usual 1/2" diameter Zeiss 1/8" stub because it would limit the FIB-SEM geometries available due to the 4.5 mm working distance associated with the FIB. Toward this goal we switched to 6-32 set screws as sample holders. We also developed a holder for the 6-32 set-screws that provide a large smooth plane allowing the specimen to be easily moved on and off the set-screw, without losing the specimen. Our first approach to this was to use a Teflon piece with a 1/8" rod (similar size to the 6-32 set-screw). However, the Teflon pieces charged up electrostatically so that the specimen moved by itself, which is not good. Using an aluminum piece with 6-32 set-screws overcame the static charging issues. We also tried a UV-curing glue however this started to cure under microscope observation, which was a problem. Similarly we tried a

thicker super glue and a 5 minute epoxy, neither of these made manipulation of the sample simple. Finally we used a very small portion of conducting double sided tape as the initial glue to hold down the specimen. In principle this allowed the specimen to be still moved once the specimen made contact with the tape. Also it got rid of any possibility of a glue wicking onto the specimen. Unfortunately this left the specimen only held to the set-screw by the double sided tape adhesive and we know this to be a drift sensitive bond. To circumvent this drift condition we used silver paint to bridge from the set-screw to the specimen in a couple of places. This took some patience because the silver paint itself can wick, however we were successful with this approach.

The coating time was thirty seconds for an average of 180 nm[1], although the coating thickness is not important when etching. The thirty seconds was defined by another student who previously worked on a similar sample. Fifteen seconds was initially tried by this student, but charging effects led him to double the coating time. Thirty seconds seems to provide good results in terms of charging, but intermediate times should be investigated on future samples. The FIB slicing and imaging were done by the Zeiss Neon; it features a 54° (non-changeable) angle between the FIB gun and the electron gun. This means that the images recorded have a slope. Two possible approaches can be used; FIBing perpendicular to the surface while imaging the sample's cross-section obliquely, or FIBing parallel to the surface while imaging the top surface obliquely. Both approaches were used and will be presented in the following sections. Figure 2.5 illustrates both cases.

[1] a graduate student previously calculated that the average deposition rate was 6 nm/s.

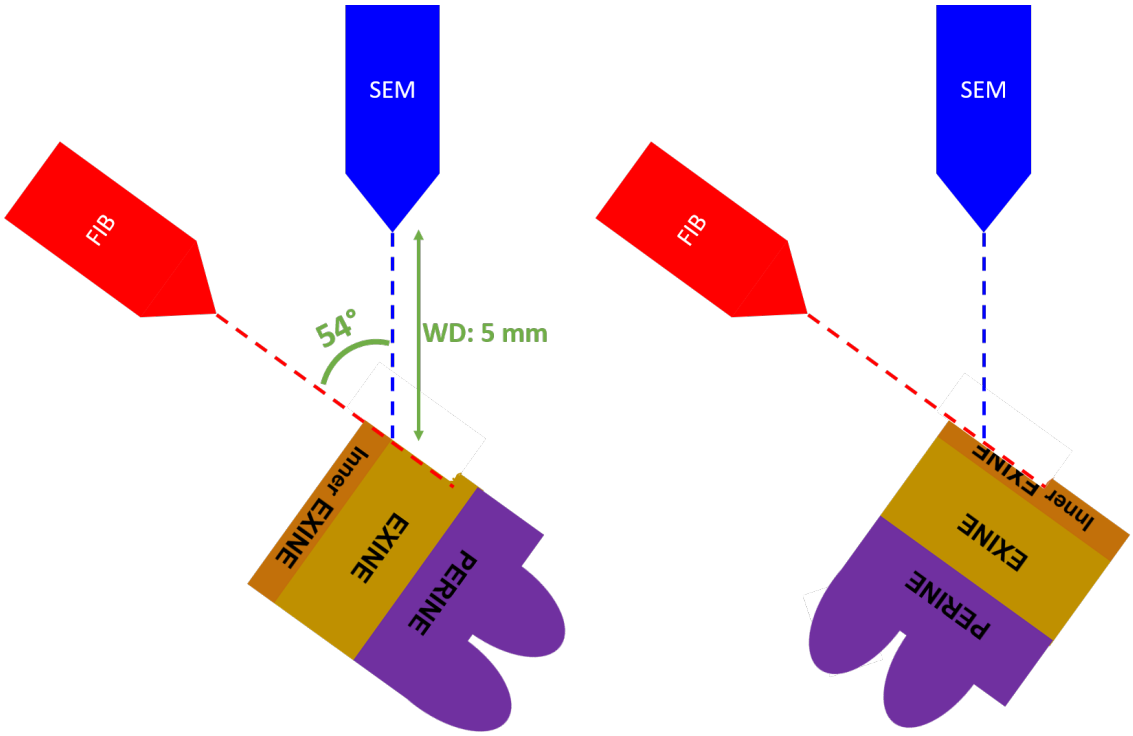

Figure 2.5: Two possible ways to obtain data from the SEM whilst etching with the FIB

3. Perpendicular Etching

The top-down etching approach was used first because of the simplicity of the approach. With this geometry one can easily create a smooth surface with a higher current before polishing with a finer current. Furthermore, viewing the inner exine cross-sectionally theoretically allows one to see a channel beginning and ending within a few slices. It is necessary to etch the entire inner exine when doing the same with parallel etching. Figure 3.1 displays the sample image by the FIB and the image acquired by SE.

A volume of 5227x3920x2690 nm^3 (pixel size of 5.104 nm) was etched using the mill for depth mode, with 10 μm as the depth. 100 picoamperes (pAs) was used as the milling current and the slicing size was modified from the auto parameter to 5.104 nm so that the voxels (3D pixels) were cubes. The images were taken with the "inlen" detector, using a magnification of 38,750 times, at speed 3, with line averaging (7.9 seconds per image).

3D reconstruction was attempted but was not successful as can be seen in figure 3.2c. The difficulty in detecting the channels resulted in the failed procedure. There were many reasons that made channel detection difficult. The main reason was the lack of dynamic range. One can observe in figure 3.1b that most of the dynamic range is taken up by the top layer of the inner exine and the bottom part of the exine; the inner exine only has a few of the grey shades avail-

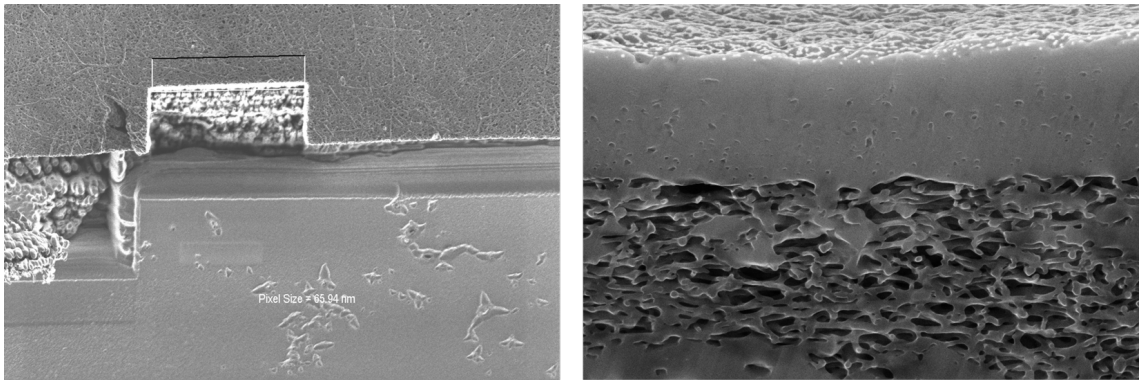

Figure 3.1: SEM (top-down) and FIB (oblique) view of the inner exine

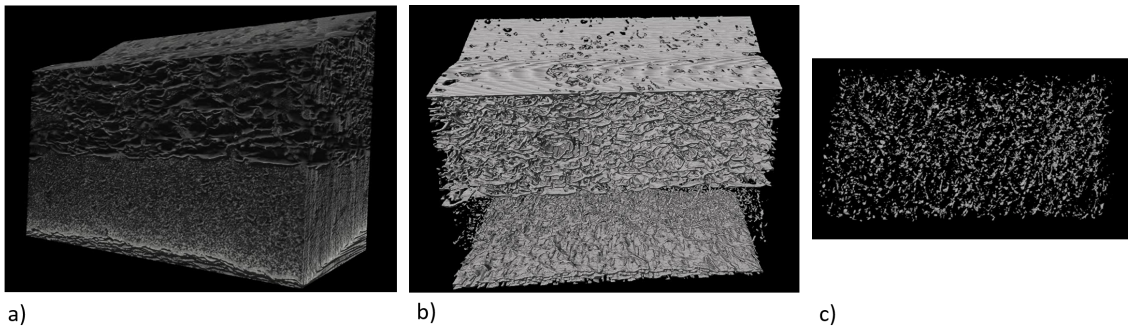

Figure 3.2: 3D images of the exine: a) using a white-black gradient. b) using a white-transparent gradient. c) only the inner exine.

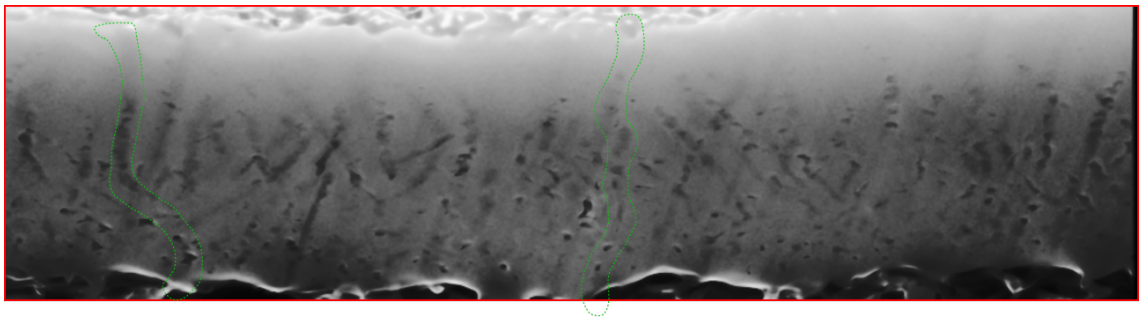

Figure 3.3: Z-projection of a substack of 27 pictures, keeping the minimum value (black pixel) in order to display channels

able, making the holes harder to detect. Additionally, the acceleration voltage was too high, providing a convolution of the surface topology and information behind it. The channels can be seen in darker shades before opening. The difference between an open channel and a future opening is very subtle and hard to differentiate. Moreover, the FIB also leaves repetitive oblique marks whilst etching hardens the differentiation process —even to the human eye.

Following the channels as they opened was also attempted manually. This was not an easy process because the channel openings are not continuous and can happen at any point on the channel. This makes it difficult to be sure that the openings found belong to the same channel. Additionally, no channel seemed to go totally through. It could not be stated whether or not the pores were connecting through because the bright edge effect occurring at the end of the inner exine decreased the contrast. Several almost connected channels were found. A Z-projection using the minimum (i.e. darker) value was used to display those channels. The picture obtained can be seen in figure 3.3 and the shadow above the circled channels suggests a pore connection. However, there is no concrete evidence.

Instead of redoing the experiment with better parameters, the second approach,

parallel etching, was used. This approach was chosen because following the channels while etching would make it easier to distinguish different channels and their path. Additionally, the shadowed marks would not exist in this configuration because all the channels are more or less perpendicular to the surface. Also, the dynamic range should not be an issue in this configuration if it is set correctly at the beginning of the procedure. Finally, in this configuration there would not be any bright edge effect dimming the contrast; only the channels should be highlighted by this effect.

4. Parallel Etching

In addition to the advantages listed in the previous section, parallel etching also offers the possibility for statistical analysis of the channels. Being in the plane of the pores allows one to count their number and see their behaviour quite easily.

The parameters used were not very different. The FIB current, depth, imagining detector, and scanning speed were left unchanged. The only difference was the break in the cubic voxel rule. Because of the top-down imaging configuration, all of the inner exine needed to be etched. Thus, it was decided to break the rule that facilitate 3D reconstruction. Not doing so would lead to extremely long operating times, estimated to be over eleven hours. The magnification was set to 37,240 times (3 nm pixel size). The width of the etched slices was set to the "auto" parameter, setting it to 14.5 nm. This significantly sped up the process, which only took about two hours and fifteen minutes.

The geometry however was not exactly as intended. Because of the curvature of the sample and the difficulty in finding a good orientation, the etching was not completely perpendicular. Instead, the etching was at an angle which caused the top of the pictures to be deeper than the bottom. A schematic representation of the geometry is represented in 4.1. The first issue to be evaluated was whether the pores were connected to the surface. To do so, an orthogonal (YZ, c.f. Figure

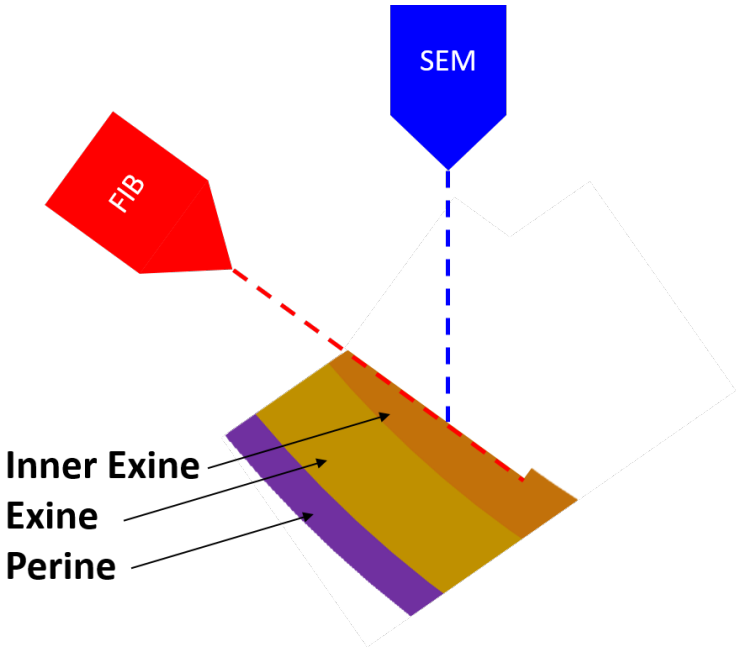

Figure 4.1: Parallel etching geometry.

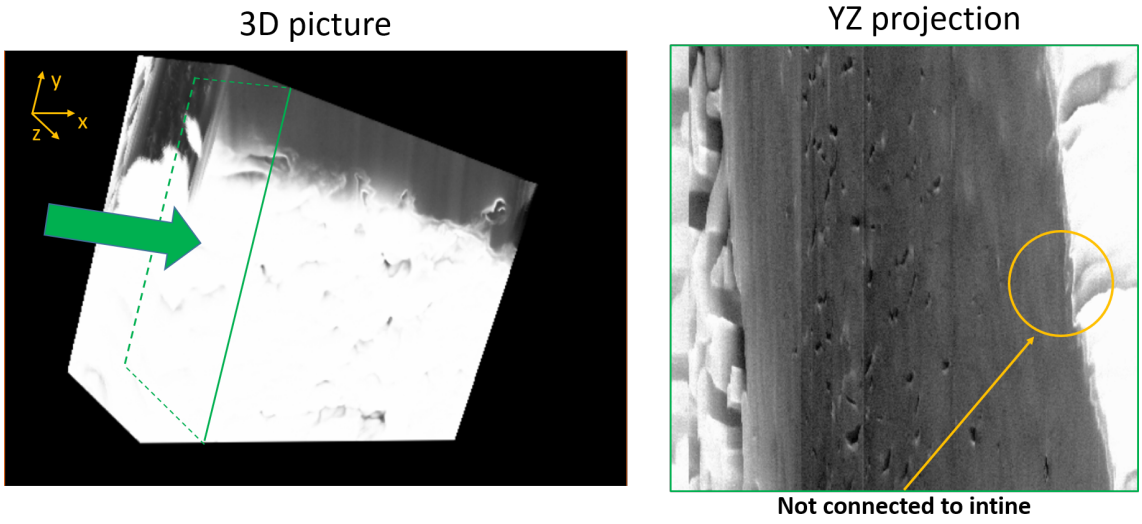

Figure 4.2: YZ projection that displays the discontinuity of the intine-side channels.

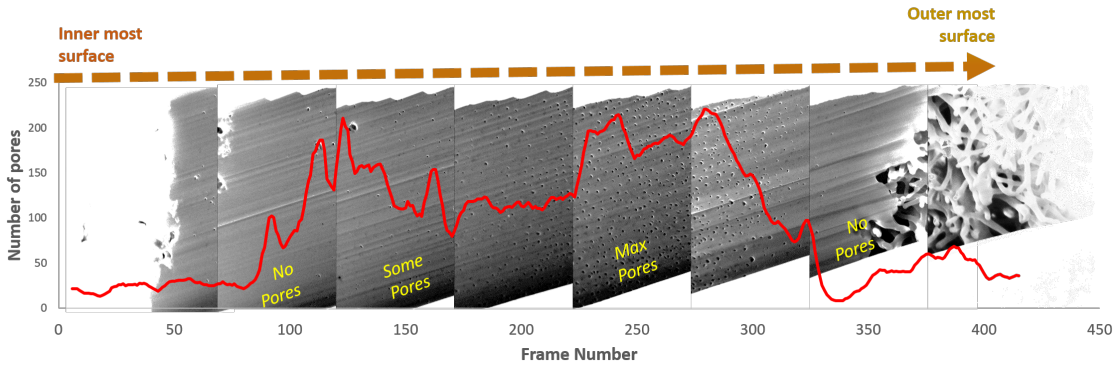

Figure 4.3: The evolution of the number of channels from the intine side (image 0) to the exine side (image $\tilde{3}70$).

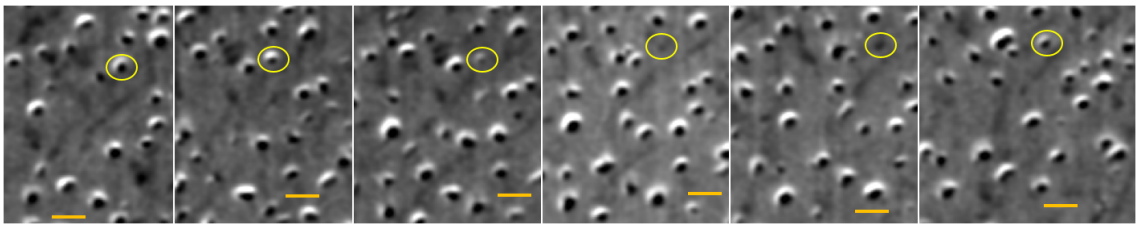

Figure 4.4: Set of pictures displaying pores closing and reopening. Each picture is separated by 14.5 nm. The scale bar is 200 nm.

4.2) projection was used. It is now clear that there is no correlation between the outside opening being visible and the inner exine pores. In fact, the data suggest that the channel number is not constant and goes from zero, to a few, to many, to a few again before disappearing just before the connection to the exine. This behaviour is better represented in Figure 4.3. 3D reconstruction was attempted in order to observe the pores' behaviours and determine whether they merge or simply disappear. The output is presented in Figure 4.5. From the data obtained, it seems that the pores are not continuous even in the high density area. The non-filtered data display the same behaviours. Indeed, it can be seen in figure 4.4 that the pores close before reopening within 43 nm. Further investigations were made on these channels to determine that low energy backscattered electrons show white features on the pores located near the intine.

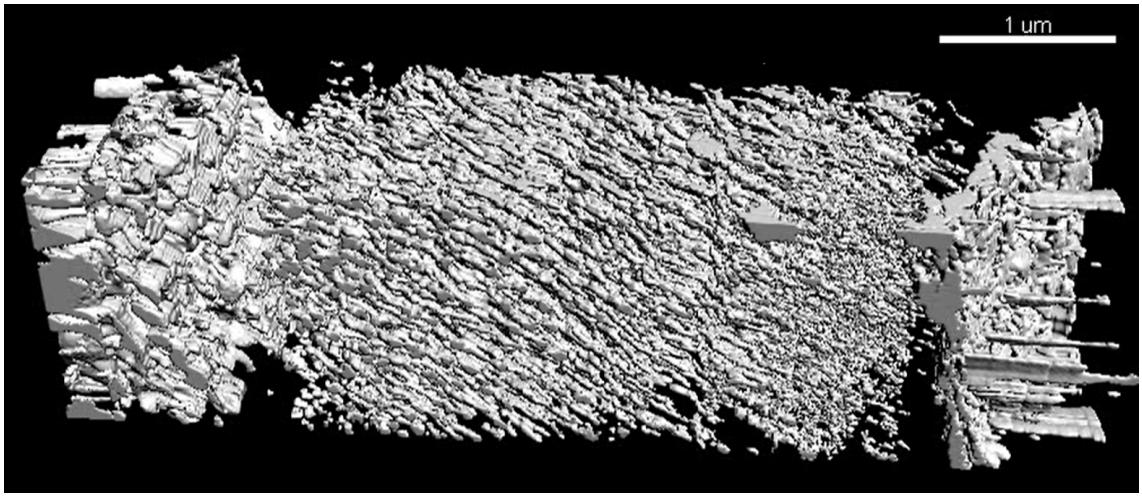

Figure 4.5: 3D reconstruction of the parallel etching data.

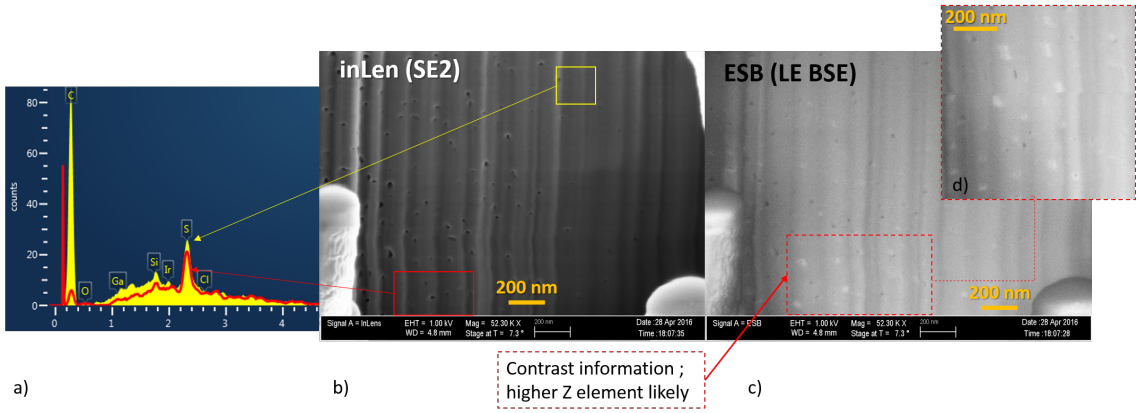

Figure 4.6: (a) is the EDS spectrum of two areas highlighted in (b), the red spectrum is located where the white marks are. (b) is an inlen (SE2) picture to compare with (c), is a low energy backscattered electron image (LE BSE) featuring white marks on the lower channels. (d) is a higher magnitude picture of (b) white marks.

This is likely due to a higher atomic number, but EDS analyses does not display any notable difference in compositions —only the carbon counts change. Both spectrum, the area they were taken, and the white marks are displayed in Figure 4.6. The fact that EDS do not present any differences in the composition could be attributed to the large interaction volume of the X-rays. This does not prove the absence of any other material obscuring the channels, although the location of those marks (near from the intine) indicates that further channels might be filled with sporopollenin.

5. Conclusion

Moving from a traditional SEM/TEM characterisation method to a SEM/SEM+FIB was studied. The FIB method showed some potential benefits and could significantly reduce preparation time. Additionally, the ability to provide 3D information about the sample's structure could be of great use and cannot be obtained from TEM. The preparation protocol should be enhanced —especially the gluing procedure— but etching parallel to the exine surface provided some data that are usable. The present work showed a discontinuity of the channels at both of the inner exine edges. Furthermore, the number of pores has been shown to vary withing the inner exine with discontinuities. The current state of the research provides no evidence that the channels are obstructed by any other material than sporopollenin —the exine material. Finally, data from the sample are available and could be used to do statistical analysis over the channels.

References

[1] Liu Quanhua, Miao Qinxian, Liu Jue, J., and Yang Wenli. Solar and wind energy resources and prediction. *Journal of Renewable and Sustainable Energy*, 1, 2009. http://dx.doi.org/10.1063/1.3168403.

[2] Martin A. Green. Third generation photovoltaics: Ultra-high conversion efficiency at low cost. *Progress in Photovoltaics: Research and Applications*, 9, 2001. http://onlinelibrary.wiley.com/doi/10.1002/pip.360/abstract.

[3] K.M. Gupta and Nish Gupta. *Advanced Semiconducting Materials and Devices*. Springer, 2015. DOI: 10.1007/978-3-319-19758-6 ; Hardcover ISBN : 978-3-319-19757-9.

[4] M. Levy, Y. and C. Honsberg. Nanostructured absorbers for multiple transition solar cells. *IEEE Transactions on Electron Devices*, 55:706–711, 2008.

[5] M. C. Debnath, T. D. Mishima, M. B. Santos, Y. Cheng, V. R. Whiteside, I. R. Sellers, K. Hossain, R. B. Laghumavarapu, B. L. Liang, and D. L. Huffaker. High-density inas/gaas1-xsbx quantum-dot structures grown by molecular beam epitaxy for use in intermediate band solar cells. *Journal of Applied Physics*, 119(11), 2016.

[6] Richard Lupia. Megaspores and palynomorphs from the lower potomac group of maryland, u.s.a. *International Journal of Plant Sciences*, 165(4):651–670, 2004.

[7] Ruth A. Stockey Gar W. Rothwell. The role of hydropteris pinnata gen. et. sp. nov. in reconstructing the cladistics of heterosporous ferns. *American Journal of Botany*, 81(4):479–492, 1994.

[8] Pryer and K.M. Phylogeny of marsileaceous ferns and relationships of the fossil hydropteris pinnata reconsidered. *American Journal of Botany*, 160:931–954, 1999.

[9] Kathleen M. Pryer, Harald Schneider, Alan R. Smith, Raymond Cranfill, Paul G. Wolf, Jeffrey S. Hunt, and Sedonia D. Sipes. Horsetails and ferns are a monophyletic group and the closest living relatives to seed plants. *Nature*, 409:618–622, 2001.

[10] Africa's renewable future: the path to sustainable growth. *IRENA publications*, 2013. `http://www.irena.org/DocumentDownloads/Publications/Africa_renewable_future.pdf`.

[11] 2015 united nations climate change conference. `https://en.wikipedia.org/wiki/2015_United_Nations_Climate_Change_Conference`.

[12] John Perlin. *Let It Shine: The 6,000-Year Story of Solar Energy.* New World Library; Revised Edition edition, 2013.

[13] D. M. Chapin, C. S. Fuller, and G. L. Pearson. A new silicon p-n junction photocell for converting solar radiation into electrical power. *Journal of Applied Physics*, 25(5):676–677, 1954.

[14] US Department of Energy. The history of solar, jun 2015. https://www1.eere.energy.gov/solar/pdfs/solar_timeline.pdf.

[15] William Shockley and Hans J. Queisser. Detailed balance limit of efficiency of p-n junction solar cells. *Journal of Applied Physics*, 32(3):510–519, 1961.

[16] O. D. Miller, E. Yablonovitch, and S. R. Kurtz. Strong internal and external luminescence as solar cells approach the shockley x2013;queisser limit. *IEEE Journal of Photovoltaics*, 2(3):303–311, July 2012.

[17] A. Marti, L. Cuadra, and A. Luque. Partial filling of a quantum dot intermediate band for solar cells. *IEEE Transactions on Electron Devices*, 48(10):2394–2399, Oct 2001.

[18] E. Chukwuocha, T.Onyeaju, and T. Harry. Theoretical studies on the effect of confinement on quantum dots using the brus equation. *World Journal of Condensed Matter Physics*, 2, 2012. http://file.scirp.org/Html/9-4800080_19097.htm.

[19] Ebrahim Jasim Khalil. *Solar Cells - New Approaches and Reviews*. Prof. Leonid A. Kosyachenko (Ed.), ISBN: 978-953-51-2184-8, InTech, 2015. http://www.intechopen.com/books/solar-cells-new-approaches-and-reviews/quantum-dots-solar-cells.

[20] S. Perkowitz. *Optical Characterization of Semiconductors: Infrared, Raman, and Photoluminescence Spectroscopy*. Academic Press, 1993.

[21] M. Grundmann, O. Stier, and D. Bimberg. Inas/gaas pyramidal quantum dots: Strain distribution, optical phonons, and electronic structure. *Phys. Rev. B*, 52:11969–11981, Oct 1995.

[22] N. Lopez, A. Marti, A. Luque, C. Stanley, C. Farmer, and P. Diaz. Experimental analysis of the operation of quantum dot intermediate band solar cells. *Journal of Solar Energy Engineering-Transactions of the Asme*, 129(3):319–322, 2007. https://www.researchgate.net/profile/Antonio_Marti2/publication/29816166_Experimental_analysis_of_the_operation_of_quantum_dot_intermediate_band_solar_cells/links/0046352a1c96f154ac000000.pdf#page=65.

[23] H. Liu, Y., M. M. Steer, J., Badcock, D. Mowbray, J., and D. Skolnick, S. Long-wavelength light emission and lasing from inas/gaas quantum dots covered by a gaassb strain-reducing layer. *Applied Physics Letters*, 86, 2005.

[24] Y. Cheng, M. Fukuda, V.R. Whiteside, M.C. Debnath, P.J. Vallely, T.D. Mishima, M.B. Santos, K. Hossain, S. Hatch, H.Y. Liu, and I.R. Sellers. Investigation of inas/gaas(1-x)sb(x) quantum dots for applications in intermediate band solar cells. *Solar Energy Materials and Solar Cells*, 147:94 – 100, 2016.

[25] David Nečas and Petr Klapetek. Gwyddion: an open-source software for SPM data analysis. *Central European Journal of Physics*, 10:181–188, 2012.

[26] Luis Pedro Coelho. Mahotas: Open source software for scriptable computer vision. *Journal of Open Research Software*, 1, July 2013.

[27] Andras E. VLADAR, Michael T. POSTEK, and Ronald VANE. Active monitoring and control of electron beam induced contamination. *SPIE proceedings series*, 2001. ftp://ftp.nist.gov/pub/mel/andras/Contamination/SPIE%20Contami%20paper.pdf.

[28] Michael T. Postek, Andras Vladar, and Petr Cizmar. Nanomanufacturing concerns about measurements made in the sem part iii: Vibration and drift. *NIST Manuscript Publication Search*, 2014.

[29] R. Songmuang, S. Kiravittaya, and O.G. Schmidt. Shape evolution of inas quantum dots during overgrowth. *Journal of Crystal Growth*, 249(3–4):416 – 421, 2003.

[30] H. Liu, Y., M. M. Steer, J., Badcock, D. Mowbray, J., and D. Skolnick, S. Determination of the shape and indium distribution of low-growth-rate inas quantum dots by cross-sectional scanning tunneling microscopy. *Applied Physics Letters*, 81:1708, 2002.

[31] Omniprobe website. `https://www.emsdiasum.com/microscopy/products/nanomanipulation/lift_out.aspx`. Accessed: 2016.

[32] Á Barna, B Pécz, and M Menyhard. Tem sample preparation by ion milling/amorphization. *Micron*, 30(3):267 – 276, 1999.

[33] Joachim Mayer, Lucille A. Giannuzzi, Takeo Kamino, and Joseph Michael. Tem sample preparation and fib-induced damage. *MRS Bulletin*, 32:400–407, 5 2007.

[34] David J. Batten, Rita J. Dutta, and Erwin Knobloch. Differentiation, affinities and palsignificance of the megaspores arcellites and bohemisporites in wealden and other cretaceous successions. *Cretaceous Research*, 17(1):39 – 65, 1996.